Utrecht University

Msc thesis

Seismic signature of water in the mantle transition zone

Author:
Vincent Thio

Supervisors:
Dr Laura Cobden
Prof. Dr Jeannot Trampert

August 21, 2014

Abstract

Though water has a major influence on tectonic and other geodynamic processes, little is known about its quantity and distribution within the deep Earth. In the last few decades, laboratory experiments on nominally anhydrous minerals (NAMs) of the transition zone have shown that these minerals can contain significant amounts of water, up to 3.3 wt%. In this study, we investigate if it is possible to use seismic observations to distinguish between a hydrous and anhydrous transition zone, by studying the relationship between mineral experimental data and seismic structures of the transition zone. We perform an extensive literature search, to generate a compilation of the water storage capacities, elastic parameters and phase boundary data for potentially hydrous minerals in the transition zone, and use thermodynamic modelling to compute synthetic seismic profiles of density, V_P and V_S at transition zone temperatures and pressures. We find that large uncertainties on the mineral phase equilibria (ca. 2 GPa) and elastic properties produce a wide range of seismic profiles. In particular, there is a lack of data at temperatures expected at transition zone pressures. Comparing our hydrous transition zone models with equivalent profiles at anhydrous conditions, we see that the depths of the 410 and 660 discontinuities cannot at present be used to map the water content of the transition zone due to these uncertainties. A better constraint may be given by the average velocities and in particular the average velocity gradients of the mantle transition zone, which decrease and increase, respectively, with increasing water content. We also find that, given our inability to constrain the depths of the 410 and 660 discontinuities at high temperatures, it is not possible to distinguish thermal from water effects, because in general their other seismic properties trade off with each other perfectly. This implies that the conventional view of a slow and thick transition zone for water and slow and thin transition zone for high temperature may not be correct. We suggest that further experiments in mineral physics should primarily focus on better constraining the phase transitions between hydrous olivine and its high-pressure polymorphs. Additionally, the uncertainties on the elastic mineral properties could be reduced significantly if data on the correlations between bulk and shear moduli and their corresponding pressure derivatives would be published.

1 Introduction

One of the prime characteristics that distinguishes the Earth from other terrestrial planets is the substantial amount of liquid water at its surface. Water plays a major role in the dynamics of our planet and is fundamental to the existence of organic life. Yet while the water cycle at the earth's surface and atmosphere is widely studied and understood, little is known about the quantity, distribution and behavior of water within the Earth. We know that water enters the mantle via subduction and is released via volcanism, but precisely how it cycles between those places is essentially unknown. Water has a large influence on the physical properties of rocks. It reduces their strength, viscosity and melting point (Chen et al., 1998; Hirschmann, 2006), which in turn yields major consequences for large-scale processes such as volcanic activity, plate tectonics (Regenauer-Lieb et al., 2001) and possibly the generation of very deep (400-600km) earthquakes (Richard et al., 2007). Therefore, in order to gain a better understanding of these processes, it is essential to constrain how much water is stored in the mantle and its distribution. This, in turn, requires us to determine the change in water solubility with respect to pressure, temperature and mineral type, and the effect which water has on the physical properties of mantle minerals.

The present-day total water volume found in oceans is about 0.025% of the total mass of the Earth, but this fraction may have been significantly higher during the early stages of the Earth's existence, ∼4.5 billion years ago (Drake, 2005). This poses the question of what happened to the excess water; did it escape the atmosphere into space, or is a significant amount of water currently stored within the deep Earth? Field studies provide both supporting and opposing results for the latter: A recent study by Pearson et al. (2014) on a ringwoodite inclusion in a diamond found that the ringwoodite had a water content of 1.5wt%, indicating that the mantle is (at least locally) subject to hydration. On the other hand, geochemical analysis of volcanic rocks by Dixon et al. (2002), together with numerical models of the deep mantle by Rupke et al. (2006), suggests that the deeper mantle is predominantly anhydrous.

Laboratory experiments in the last two decades on the water storage capacity of major mantle minerals previously thought to be anhydrous, the so called 'nominally anhydrous minerals' (NAMs), have shown that they actually have the capacity to absorb small weight percentages of water, in the form of structurally bound (OH^-) ions. When integrated over the whole volume of the Earth, the mantle could therefore, theoretically, contain significant amounts of water, up to several times the total water volume currently found in the oceans (Smyth and Jacobsen, 2006). Two minerals in particular, wadsleyite and ringwoodite, have been found to have a significant water storage capacity of up to several weight percent (e.g. Chen et al., 2002; Ohtani et al., 2000). These high-pressure polymorphs of olivine make up about 60% of the transition zone, a region in the mantle between approximately 410 and 660 km depth which is characterized by high velocity gradients. The transition zone is bounded on both sides by sharp increases in velocity, the so called '410' and '660' discontinuities, which are thought to arise from the phase transition of olivine to wadsleyite (α-$[Mg,Fe]_2SiO_4 \rightarrow \beta$-$[Mg,Fe]_2SiO_4$) and the decomposition of ringwoodite into perovskite and magnesiowustite (γ-$[Mg,Fe]_2SiO_4 \rightarrow [Mg,Fe]SiO_3 + [Mg,Fe]O$), respectively. Since wadsleyite and ringwoodite have much greater water storage capacity than the overlying olivine or underlying perovskite, the transition zone could be a major water reservoir, where water entering the mantle by subduction becomes trapped between the relatively dry minerals above and below the transition zone (the so-called 'transition-zone water filter' of Bercovici and Karato, 2003).

Constraints on the physical properties of the mantle are predominantly obtained from seismic observations. Three main structural aspects of the transition zone are expected to be influenced by

water and might be seen in seismic data: These are (1) The velocity profile of the transition zone, (2) the position (i.e. depth) of the '410' and '660' discontinuities and (3) the impedance contrast at the '410' and '660' discontinuities. Experiments on the elastic properties of NAMs indicate that both P and S wave speed decrease with increasing water content (e.g. Manghnani et al., 2005; Ye et al., 2012). This implies that the average velocity in the hydrous transition zone will be lower than at anhydrous conditions, and that the impedance contrast at the '410' and '660' discontinuities will decrease and increase, respectively, assuming that the minerals above and below the transition zone contain significantly less water. Studies on the phase transitions between olivine and its high-pressure polymorphs indicate that the olivine-wadsleyite transition occurs at slightly lower pressures (Smyth and Frost (2002)) under hydrous conditions, and the post-spinel composition at slightly higher pressures (e.g. Litasov et al., 2005; Ghosh et al., 2013).

However, mapping the water content inside the transition zone using seismology is non-trivial for two main reasons. Firstly the seismic structure is also modified by changes in temperature and composition (e.g. Fe content), meaning that there may be a non-unique physical interpretation for a given seismic structure. Secondly the seismic data themselves each have uncertainties and limited resolving power, and in light of this it is unclear if the differences in seismic structure between anhydrous and hydrous transition zone regions are significant enough to be resolved by seismology.

In this study, we use data from mineral physics experiments on hydrous NAMs to compute density and velocity profiles through the transition zone at hydrous conditions. We do this in order to quantify the effect of water on the density and velocities at the '410', '660' and within the transition zone, relative to uncertainties on the data and changes in temperature and composition. We compare our findings to real seismic observations to investigate whether seismic observations have the capacity to identify water inside the mantle transition zone.

2 Theoretical background

In order to calculate the seismic properties of a hydrous transition zone, we need to know the elastic properties of the constituent minerals at every pressure and temperature within the transition zone. In this chapter we summarize the theoretical background necessary to constrain the elastic properties from experimental data, and give an outline of how the seismic structure is computed from these elastic properties.

2.1 Equation of state

The wavespeed of a single mineral can be calculated for V_P and V_S respectively,

$$v_P = \sqrt{\frac{K + \frac{4}{3}G}{\rho}} \qquad v_S = \sqrt{\frac{G}{\rho}} \tag{1}$$

where ρ is the density, K the bulk modulus, G the shear modulus, each depending on the pressure and temperature. Since these elastic properties have not been measured at every possible P-T point appropriate for the mantle, we need an alternative method to constrain them. To this end, we use an equation of state (EoS) that defines how to extrapolate the elastic properties at ambient conditions to high pressure and temperature. We use a third-order finite strain EoS (the $Birch - Murnaghan$

formulation, e.g. see Poirier (2000) for a full description) to extrapolate from 0 GPa to high pressure at constant temperature, and then add a Mie-Gruneisen thermal pressure correction to extrapolate from 298 K to high temperature, following Stixrude and Lithgow-Bertelloni (2005).

2.2 Wave speed at single P-T point

For each P-T point, we compute the overall wave speed by taking the weighted average of ρ, K and G of each stable mineral at that point. For the density we use a Voigt average, which is calculated by

$$\rho_{Voigt} = \sum_{i=1}^{N} \rho_i \cdot V_i \tag{2}$$

where ρ_{Voigt} is the Voigt average density, V_i and ρ_i the volume fraction and density of the ith' mineral, and N the number of stable minerals. The bulk and shear moduli are calculated using a Voigt-Reuss-Hill (VRH) averaging scheme,

$$f_{VRH} = \frac{1}{2}[f_{Voigt} + f_{Reuss}], \qquad \frac{1}{f_{Reuss}} = \sum_{i=1}^{N} \frac{f_i}{V_i} \tag{3}$$

where f is the elastic property (K or G), f_{VRH} the VRH average property value, f_i the elastic property value of the ith mineral and f_{Voigt} the Voigt average (Equation 2).

2.3 The *Perple_x* program

The computer program *Perplex_X* (Connolly, 1990, 2005) is used to solve the EoS. For given bulk composition, set of mineral elastic properties and pressure-temperature range, *Perplex_X* applies the EoS to derive the elastic properties per mineral at each point within a 2D-grid of pressure and temperature points. Simultaneously, *Perple_x* computes the stable mineral assemblage at each P-T point via a free energy minimization. It then calculates the VRH-average wavespeeds along an input P-T path by interpolation of the local elastic properties at the nearest grid points.

The thermoelastic dataset of Stixrude and Lithgow-Bertelloni (2011) was used as the primary input for all calculations. This data set is composed of 47 minerals and mineral end-members, each described in terms of 10 thermodynamic parameters (The Helmholtz free energy (F_0), volume (V_0), bulk and shear moduli (K_{T0}, G), their pressure derivatives (K', G'), Debye temperature (θ_0), gruneisen parameter (γ), and two parameters related to the temperature derivatives of the bulk and shear moduli (q_0, η_0)). These parameters have been obtained by a global inversion of experimental data allowing seismic properties and phase equilibria to be derived within a self-consistent framework simultaneously.

There are some limitations of *Perple_x* that require attention: firstly, the NAMs that we will be altering (olivine, wadsleyite and ringwoodite) are solid solutions of Mg and Fe. Since *Perple_x* requires elastic properties of the Fe and Mg endmembers only, this requires new elastic properties for both endmembers. In general, data for pure Fe endmembers are lacking for these minerals, especially at high temperature. Secondly, *Perple_x* assumes a constant bulk composition with pressure and temperature.

2.4 Composition

The chemical compositions in our models are defined in terms of up to five oxides: MgO, FeO, SiO_2, Al_2O_3 and CaO. These oxides comprise about 98 % of the mantle volume. The base composition of our models is pyrolite, which is often assumed to be the average mantle composition (e.g. Anderson, 2007). Pyrolite assumed in this study is composed of the following molar percentages of oxide endmembers: 3.25% CaO, 6.24% FeO, 49.13% MgO, 2.77% Al_2O_3 and 38.61% SiO_2 (from Sun, 1982). For the hydrous models we assume the same pyrolitic composition: we do not add OH to the bulk composition as input to $Perple\_x$ but rather incorporate the effect of water by adjusting the elastic parameters. To account for the change in density due to water, we combine the volume (calculated by $Perple\_x$) with the molar mass of the hydrous mineral.

Two additional compositions were used to infer the seismic properties of pyrolite at hydrous conditions. A 'Fo100' composition for the elastic properties of Mg_2SiO_4 (where 'Fo' stands for forsterite), composed of [66.6% MgO, 33.3% SiO_2 (percentage in mol)], and a mixed Fe/Mg composition, composed of [60% MgO, 6.6% FeO, 33.3% SiO_2] or [53.3% MgO, 13.3% FeO,33.3% SiO_2], for Fo90 and Fo80 respectively.

2.5 Temperature-Pressure structure

We assume an adiabatic P-T path through the mantle, implying a constant entropy along the path. An adiabatic thermal structure arises if the mantle is vigorously convecting. We base our main models on an adiabat with a potential temperature of 1573 K (following Cobden et al., 2008), but hotter (1773 K) and colder (1373 K) adiabats are also considered.

3 Methods

3.1 Storage capacity mantle

Water can have a significant effect on the elastic properties of a mineral, and therefore on the velocity profile of the mantle. However, the water storage capacity differs per mineral, with some minerals having very low storage capacities (e.g. stishovite, garnet; Bolfan-Casanova et al., 2000; Aubaud et al., 2008) whereas others have capacities up to 3.8 wt% (Fe-free wadsleyite, Chen et al., 2002). Therefore, it is not realistic to assume a single water content for the whole upper mantle. Instead, we undertook a literature study of the water storage capacities of each NAM and determined the water content separately per mineral.

In this study we will focus on the water content of olivine, wadsleyite and ringwoodite, and assume all other NAMs to be anhydrous. Most other minerals are volumetrically small within the transition zone, so even if they could store large amounts of water it would most likely have little effect on the seismic profile. Garnet does occupy a large volume fraction (ca. 40%), but its low water storage capacity (less than 1 wt%, e.g. Aubaud et al., 2008) is assumed to have a small seismic effect, which is insignificant compared to the uncertainties caused by the elastic properties of the hydrous polymorphs of olivine.

3.1.1 Storage capacity per NAM

Olivine

Storage capacities of up to 0.9 wt% have been found for olivine (Smyth and Jacobsen, 2006), but are generally lower depending on pressure, temperature and Fe-content (Ferot and Bolfan-Casanova, 2012; Litasov et al., 2007; Deon et al., 2011; Zhao et al., 2004). Kohlstedt et al. (1996) found much lower values, up to 0.15 wt% in San Carlos olivine ($(Mg_{0.9}Fe_{0.1})_2SiO_4$), but Mosenfelder et al. (2006) used a different calibration method and obtained 0.64 wt% water for Fe-bearing olivine. This was also concluded by Chen et al. (2002), who investigated the storage capacity of San Carlos olivine between 12.6 and 14.6 GPa and at a temperature of 1473 K. Deon et al. (2011) tested the storage capacity at varying pressure and found a positive correlation. They also found that Fe increases the storage capacity at transition zone conditions (12.6-14.6 GPa), which agrees with low-pressure experiments done by Zhao et al. (2004), but not with Litasov et al. (2007), who observed marginally lower maximum concentration in Fe-bearing olivine (0.6-0.7 wt% at 1673K), compared to Fo100 (0.9 wt%) at the same conditions.

The effect of temperature on water storage capacity is unclear. Zhao et al. (2004), report a clear increase in solubility with increasing temperature (an increase from 1273 K to 1573 K results in more than twice the capacity), while other papers (Litasov et al., 2007; Smyth et al., 2006) conclude the opposite.

Available data for hydrous olivine is plotted in Figure 1 (top). The data clearly show an increase in water content with pressure and decrease with temperature. The difference between Fe-bearing (squares) and Fe-free (circles) olivine is not directly clear from our compiled data set, which shows contradicting information at low temperature and high pressure. The red star indicates the P-T point along the 1573 K adiabat (see also Figure 5 bottom, right) that we used to determine the average water content of saturated olivine. This average value, which is ∼0.25 wt%, was used to determine the partition coefficient between NAMs.

Wadsleyite

Wadsleyite has the highest storage capacity of the NAMs, first inferred theoretically by Smyth (1987) and later shown experimentally by Inoue et al. (1995). Since then, numerous studies have been done to determine the storage capacity of wadsleyite as a function of pressure, temperature and Fe-content (e.g. Jacobsen et al. (2005); Litasov and Ohtani (2003); Inoue et al. (2010a)). In Fe-free wadsleyite, storage capacities of up to 3.5-3.8 wt% have been found by Chen et al. (2002), who did their experiments within a pressure range of 14.2-14.7 GPa and at a constant temperature of 1473 K. For Fe-bearing wadsleyite, they found slightly lower but still significant storage capacities of 1.9-3.4 wt% at the same conditions, which agrees with values found by Kohlstedt et al. (1996) and Kawamoto et al. (1996), who report 2.4 wt% at 1373 K and 14-15 GPa and 1.52 wt% at 1773 K and 15.5GPa, respectively. Bolfan-Casanova et al. (2000), on the other hand, report much lower solubilities in wadsleyite of only 0.212 wt% at 15 GPa and 1573 K.

Demouchy et al. (2005) studied the water content of saturated Fe-free wadsleyite over a pressure range of 13-18 GPa (T = 1473 K) and temperature range 1173-1673 K (P = 15 GPa), to investigate the influence of T and P on water absorption. They found that pressure does not have a major influence, but that increasing temperature decreases the storage capacity significantly. This was also found by Litasov et al. (2011), who extended their study to higher pressure and temperature values. Important to note here is that both their studies were performed with an Fe-free composition.

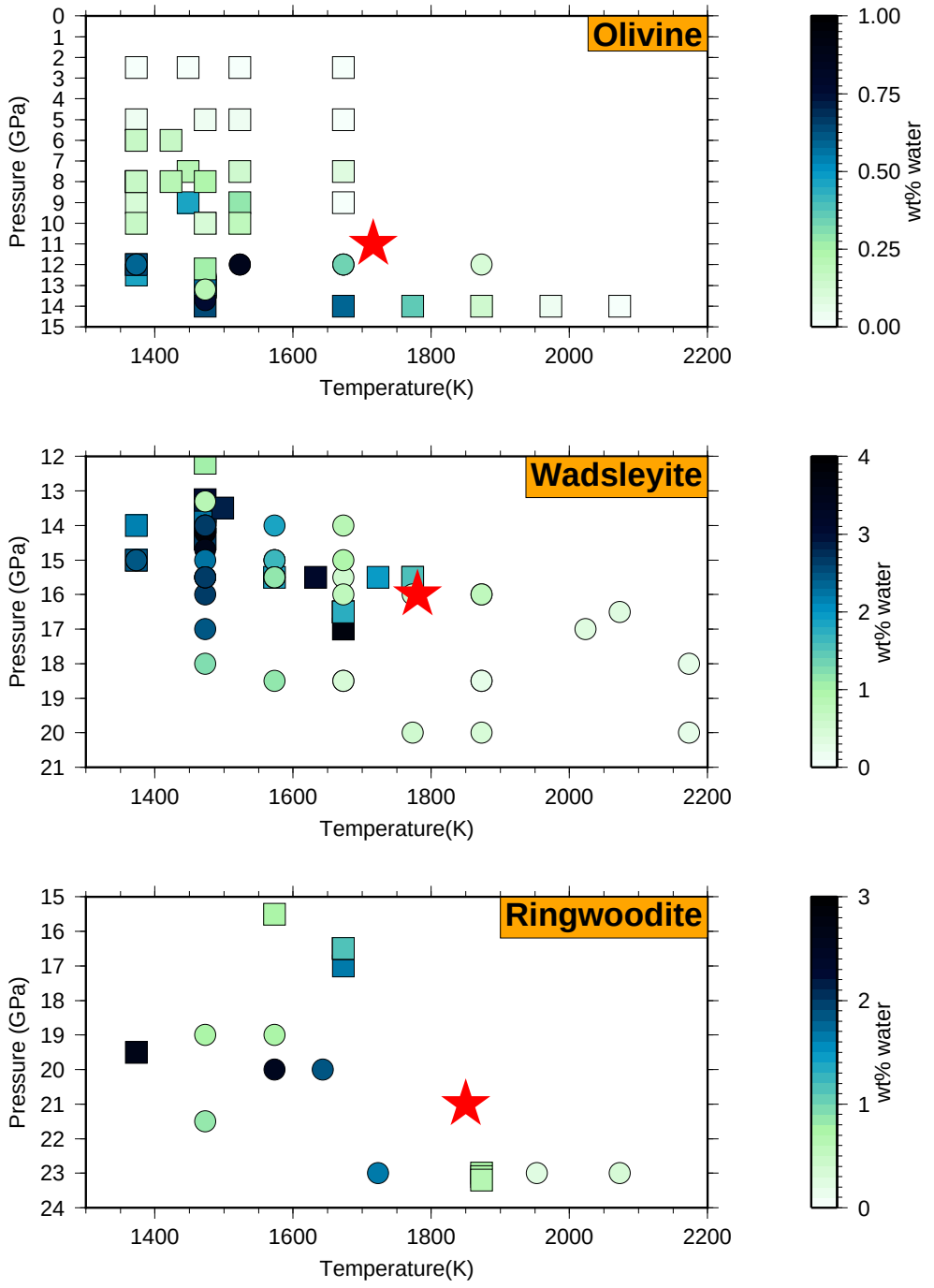

Figure 1: Water storage capacity per NAM as a function of temperature and pressure. Circles indicate Fe-free samples, squares indicate Fe-bearing samples. The red stars indicate median pressure and temperature per phase in its field of stability along the 1573 K adiabat in pyrolite, below 300 km depth. These P-T points correspond to those indicated in Figure 5 (bottom,right). Data are taken from Bolfan-Casanova et al. (2000); Chen et al. (2002); Demouchy et al. (2005); Deon et al. (2011); Ferot and Bolfan-Casanova (2012); Inoue et al. (1995, 2010a); Kawamoto et al. (1996); Kohlstedt et al. (1996); Litasov and Ohtani (2003); Litasov et al. (2007, 2011); Mosenfelder et al. (2006); Ohtani et al. (2000); Smyth and Jacobsen (2006).

Figure 1 (middle) shows available data for water content of wadsleyite as a function of temperature and pressure. At 1473 K, the storage capacities of Fe-free (circles) and Fe-bearing (squares) wadsleyite are roughly the same, but a significant decrease occurs for Fe-free wadsleyite at higher temperatures, whereas only a slight decrease occurs in the the Fe-bearing compositions. The red star indicating the average pressure and temperature of saturated wadsleyite along the 1573 K adiabat, corresponds to a value of ∼1.5 wt%.

Ringwoodite

Ringwoodite has the second highest water storage capacity after wadsleyite, with a wt% reportedly up to 2.7% (Kohlstedt et al., 1996). A negative correlation with temperature was found for both Fe-free (Ohtani et al., 2000) and Fe-bearing ringwoodite (combining the data of Inoue et al., 2010a,b; Kawamoto et al., 1996), but the pressure dependence is unclear.

Recently, Pearson et al. (2014) studied the water content of a ringwoodite inclusion in a diamond, thought to have originated in the transition zone. They found a water content of 1.5 wt%, which suggests that ringwoodite is indeed (locally) hydrous within the transition zone.

A compilation of the data from these and other papers is shown in Figure 1 (bottom), for Fe-free (circles) and Fe-bearing (squares) ringwoodite respectively. The average pressure and temperature of ringwoodite along the 1573 adiabat, indicated by the red star, yields an average value of ∼0.8 wt%.

Perovksite

Experiments indicate that perovskite can store much smaller amounts of water compared to the other NAMs, with reported values of 0.01 wt% (Litasov and Ohtani, 2003), 0.05 wt% (Higo et al., 2006) and <∼0.1 wt% water (Inoue et al., 2010a). Furthermore, recent experiments have shown that adding water to perovskite causes the water to sit on grain boundaries or in fluid inclusions rather than being incorporated into the crystal structure (J. Jackson, personal communication 2014). In our models, we assume anhydrous perovskite since data on the elastic properties of hydrous perovskite are not yet available, but in any case it is likely that the low water solubility produces insignificant/minor changes in seismic properties.

3.1.2 Partition coefficients

The water partition coefficient between two minerals specifies how the water is divided between the minerals at the phase boundary. Previous measurements of the partition coefficient of wadsleyite/olivine ($D_{wad/oli}$) vary between 1.8 to 6.0 (Smyth and Jacobsen, 2006; Litasov and Ohtani, 2008; Litasov et al., 2011; Demouchy et al., 2005; Chen et al., 2002; Inoue et al., 2010b) and of wadsleyite/ringwoodite ($D_{wad/ring}$) between 1.63 and 2.5 (Inoue et al., 2010b; Deon et al., 2011), indicating that the water partitioning is poorly constrained. In this study we derive water partition coefficients from the compiled dataset of the storage capacity per NAM (Figure 1), described in the previous section. Since we assume constant water content per NAM, we compute the water partition coefficients from the maximum expected water contents at mantle conditions. These are ∼0.25 wt%, ∼1.5 wt% and ∼0.8 wt% for olivine, wadsleyite and ringwoodite, respectively, resulting in partition coefficients $D_{wad/oli} = 6.0$ and $D_{wad/ring} = 2.0$. These values are compatible with the

results of Inoue et al. (2010b), who studied the water partitioning of a pure-Mg composition and found 5:30:15:1 for olivine:wadsleyite:ringwoodite:perovskite.

3.2 Numerical Experiments

We conducted a range of numerical experiments with varying water content and composition, assuming a 1573 K adiabatic P-T path through the mantle. Each numerical experiment consists of 10 000 runs, where the mineral properties of the NAMs vary for each run within the pre-determined uncertainty bounds as described in the following section. Since wadsleyite has the higher storage capacity of the NAMs, we pre-define the water content of wadsleyite and derive the water contents of olivine and ringwoodite by the partition coefficients (where $D_{oli:wad:ring} = 1{:}6{:}3$). Therefore, for the remainder of this study, the 'water content' of a model implies the water content of wadsleyite only.

The '410' and '660' discontinuities are primarily determined from the maximum jump of V_P within a pre-determined depth range (350-450 km for the '410', 550-700 for the '660'), and if no jump in V_P could be observed, from the jump in V_S. If a clear jump is absent for both V_P and V_S, the discontinuity is not present in that run and further data cannot be derived from that run. We only found this for some models at the higher water content (3.3 wt% water) and only at the '410' discontinuity.

3.2.1 Steps for velocity and density profile calculation

Here we summarize the steps taken to compute velocity and density profiles for a given thermochemical structure:

1. The bulk chemical composition is defined, described in terms of the molar percentage of up to 5 main oxide endmembers (MgO, SiO_2, FeO, Al_2O_3 & CaO).
2. The water content of wadsleyite is determined, water contents of olivine and ringwoodite are derived using the partition coefficients (usually 1:6:3, Section 3.1).
3. Mineral elastic properties are defined at ambient conditions. For anhydrous minerals we use the thermoelastic dataset of Stixrude and Lithgow-Bertelloni (2011) and for hydrous minerals we define our own uncertainty bounds based on the available literature.
4. The elastic parameters are extrapolated from ambient conditions to mantle pressures and temperatures for each of the minerals by *Perple_x*, using the equation of state of Stixrude and Lithgow-Bertelloni (2005).
5. Phase boundaries and mineral compositions at each P-T point on the 2D grid are calculated intrinsically within *Perple_x*, by combining the bulk chemical composition, elastic parameter P-T field per mineral (step 4) and solid solution model.
6. At each P-T point, the K, G and density of the NAMs are updated to include the effect of water on the density, which cannot be computed intrinsically (Section 3.3.3).
7. For a given 1D P-T profile (typically a 1573 K adiabat), density and velocity profiles are computed by combining the mineral assemblage (step 5) with the (updated) elastic parameters (step 4,6) at each point along the 1D path.

3.3 Elastic properties of hydrous minerals

A new dataset of elastic properties at hydrous conditions had to be defined for both the Fe and Mg endmembers of each NAM. We obtained these new parameter values primarily from experimental data, but if limited data was available we constrained these parameters either theoretically from other mineral parameters, iteratively from indirect experimental data (e.g. changing F_0 and θ_0 iteratively until the computed phase boundary matches the phase boundary from experiments) or using systematic relationships from anhydrous minerals.

3.3.1 Volume, bulk and shear modulus (V_0, K_{T0}, G_0, K', G')

For the magnesium end-member of each NAM (Mg_2SiO_4), we performed a literature search for the volume (V_0), bulk modulus (K_{T0}), shear modulus (G_0) and their pressure derivatives (K' and G') at hydrous conditions. For the other mineral parameters a literature search proved to be futile due to very limited or often complete lack of data. To compute the full range of possible property values, uncertainty bounds were taken conservatively such that most experimental data points, including their uncertainties, lie within these bounds (see Figure 3). Data falling outside these bounds either show large uncertainties or do not follow the general trend (e.g. the volume measurement for wadsleyite at 2.6 wt%).

No data was found for the elastic properties of pure Fe mineral endmembers (Fe_2SiO_4), but limited data was available for (Mg,Fe)-mixtures (typically 10-20% Fe). To determine the elastic properties for the Fe-endmembers, we used the difference between the Fe and Mg endmember values at anhydrous conditions (from Stixrude and Lithgow-Bertelloni (2011)). The elastic property at the Fe endmember as a function of water content could then be determined by extrapolating the Mg endmember along the same trend as the difference between the anhydrous Mg and Fe endmember values. The uncertainty on the Fe-endmember property at hydrous conditions is equal either to the anhydrous uncertainty (as published by Stixrude and Lithgow-Bertelloni, 2011) or the corresponding Mg-endmember uncertainty, whichever is larger. To check the validity of this method, we checked if data from hydrous (non endmember) (Mg,Fe) solid solution experiments fall within the uncertainty bounds set by this method (see Figure 2). We found that all data points fall within these bounds and thus conclude that the model is sufficiently conservative.

Figures 3 and 4 show the change in mineral property as a function of water content per NAM for the Mg- and Fe-endmembers of each mineral. The first two columns of plots show the isothermal bulk and shear moduli, respectively, at ambient pressure and temperature. They show a significant effect of water on the bulk and shear moduli, where both properties decrease with increasing water content. This decrease can be as much as one-third, in the case of fully saturated wadsleyite with a wt% water of 3.3 %.

On the other hand, the pressure derivatives of the bulk and shear modulus, plotted in the third (K') and fourth (G') columns, show an increase with increasing water content. Only for wadsleyite does the pressure derivative of the shear modulus not increase with increasing water content, but this could be due to the large uncertainty on the anhydrous value and the paucity of data at hydrous conditions. The higher pressure derivatives at hydrous conditions indicate that though the bulk and shear moduli of the hydrous NAMs at ambient conditions are lower than their anhydrous counterparts, their bulk and shear moduli might ultimately be higher within the mantle. Depending on the effect of water on the density, we may expect to see a velocity crossover when comparing anhydrous to hydrous velocity profiles, where the hydrous profile has lower velocities at shallower

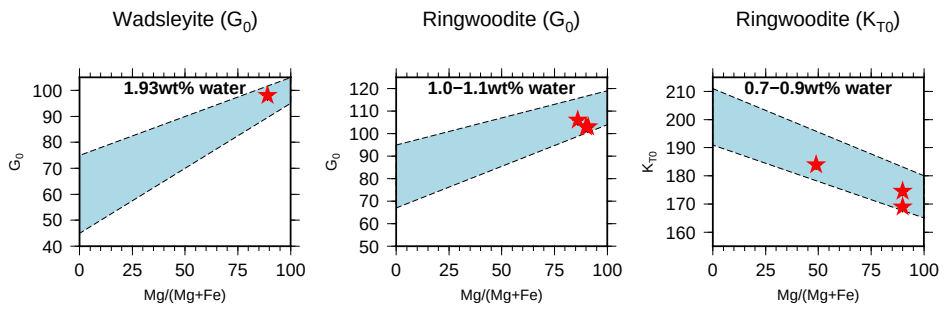

Figure 2: Non-endmember elastic properties of wadsleyite and ringwoodite at hydrous conditions. Left: G_0 of wadsleyite, middle: G_0 of ringwoodite, right: K_{T0} of ringwoodite. Red stars indicate individual measurements, blue bands the uncertainty bounds set by the uncertainties at the Mg and Fe endmembers. Exact values and associated references are shown in Tables 2-4 in Appendix A.

depth but a higher velocity gradient throughout the mantle. This idea of a velocity cross-over has previously been suggested for hydrous forsterite by Mao et al. (2010).

The last column shows the mineral volume, in cubic centimeters per mole, as a function of water content. The volume of each NAM increases in the presence of water. We suggest that the spread of data at higher water contents (most notable in ringwoodite) is probably due to different kinds of hydrogen incoporation into the crystal structure.

3.3.2 Gruneisen parameter and temperature dependence of K and G (γ, η_0, q_0)

The Gruneisen parameter and temperature dependence of the bulk and shear moduli were much harder to constrain from the literature than the pressure derivatives dK/dP and dG/dP. These parameters may be approximated with the following formulas, after Stixrude and Lithgow-Bertelloni (2005). The Gruneisen parameter γ, which is used to set limitations on the pressure and temperature dependence of thermal properties of a mineral, is given by

$$\gamma = \frac{\alpha K_T}{C_v \rho} \tag{4}$$

The q_0 can be approximated by (Anderson, 1995),

$$q_0 \approx \delta_T - K_0' + 1, \qquad \text{where } \delta_T = -(\alpha K_T)^{-1}(\partial K/\partial T)_P. \tag{5}$$

The η_{S0} value can be estimated from:

$$\frac{\eta_S}{\gamma} \approx \delta_G - K_0', \qquad \text{where } \delta_G \equiv -(\alpha K_T)^{-1}(\partial G/\partial T)_P. \tag{6}$$

Where Cv is the heat capacity at constant volume, ρ the density, α the thermal expansion coefficient, Kt the bulk modulus, K' the pressure derivative of the bulk modulus, and dK/dT and dG/dT the temperature derivatives of K and G respectively. We found temperature derivatives for the bulk and shear moduli to range from -0.038 to -0.015 for ringwoodite (Mao et al., 2012; Smyth and Jacobsen, 2006) and between -0.019 for wadsleyite. Values for the thermal expansion coefficient

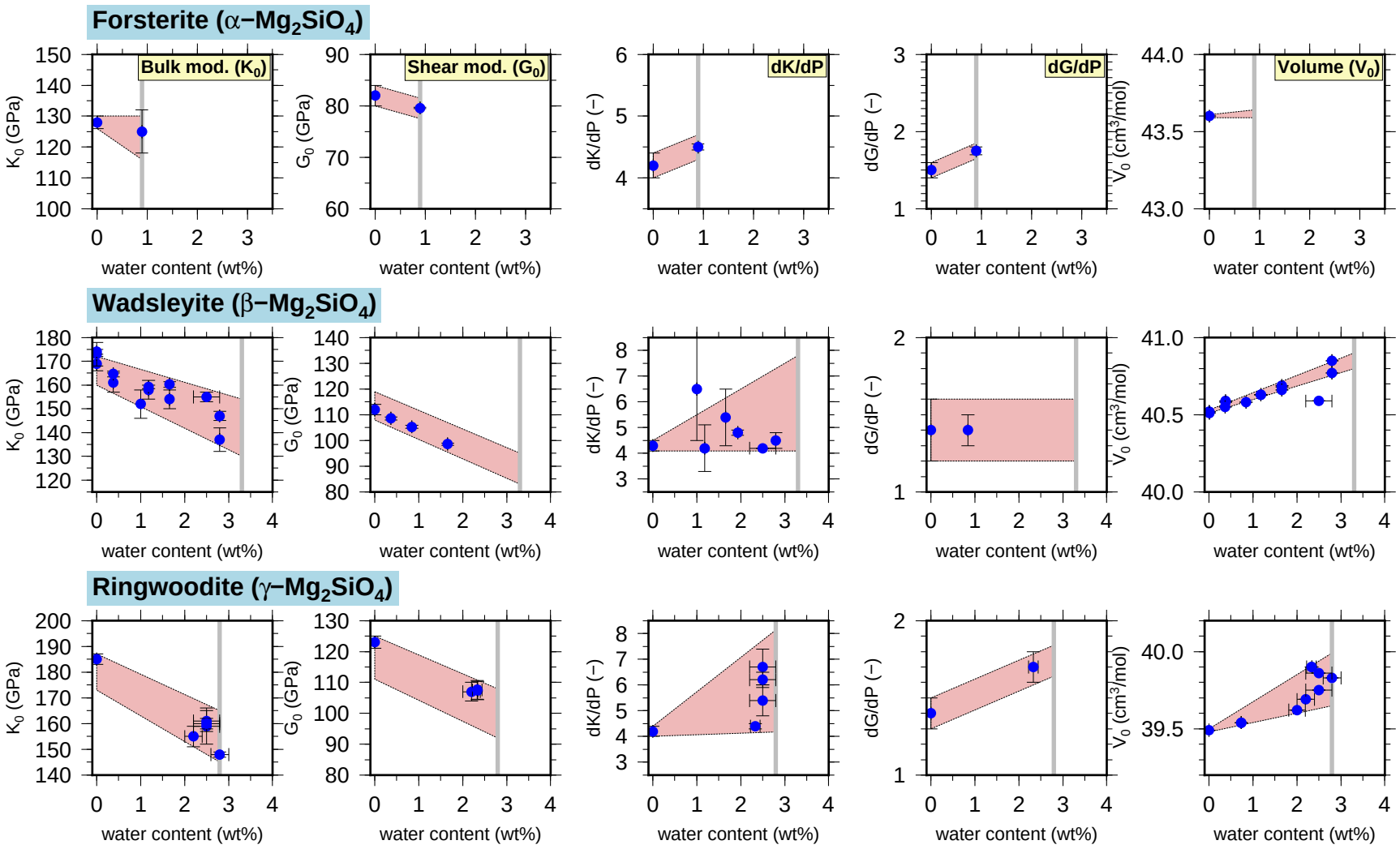

Figure 3: Elastic properties at the Mg-endmember of olivine (forsterite), wadsleyite and ringwoodite. Blue circles correspond to experimental data (See Tables 2-4 in Appendix A for references), the grey lines indicate maximum water content per mineral. The pink area shows the uncertainty ranges assigned to each parameter in our calculations.

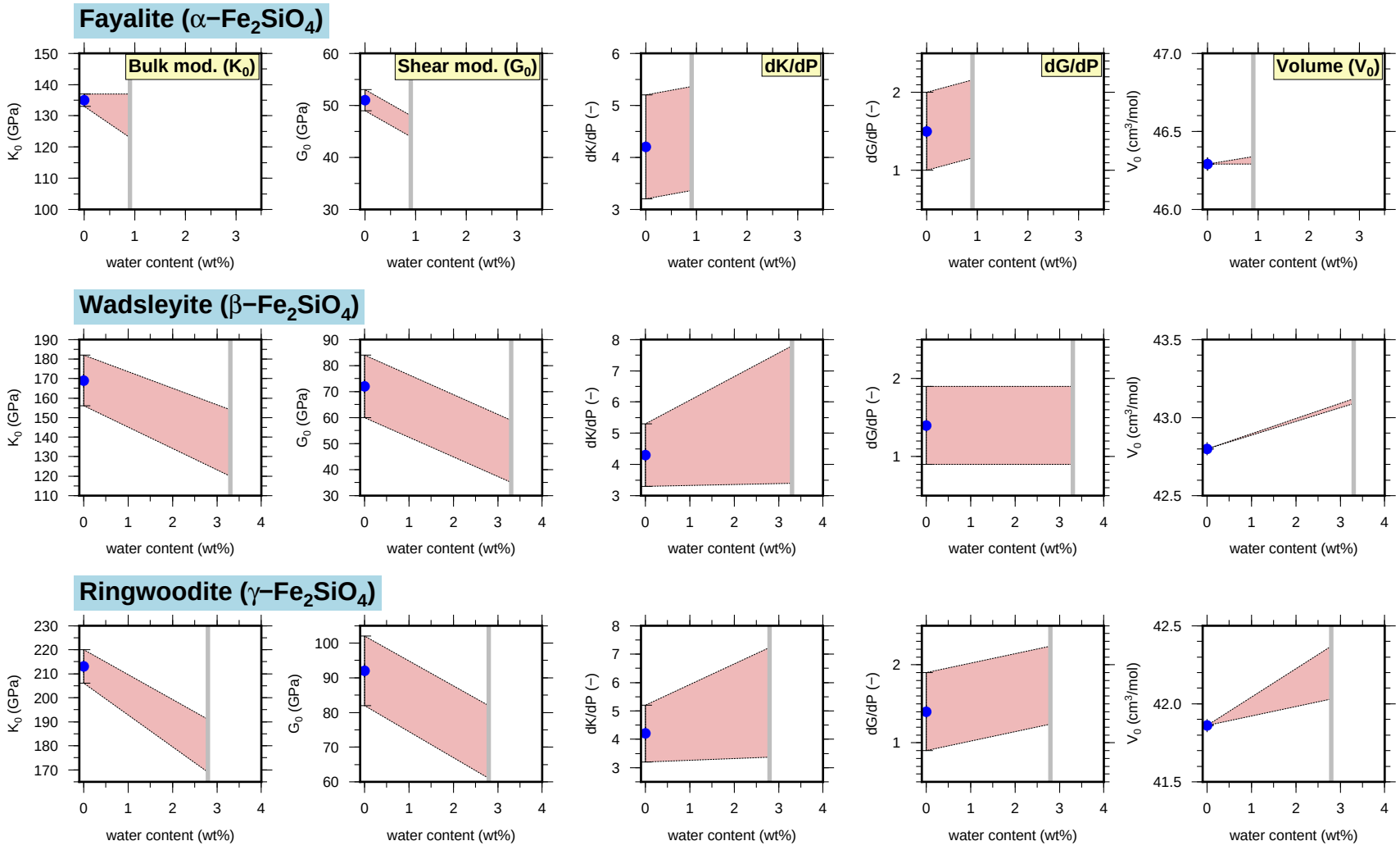

Figure 4: Elastic properties at the Fe-endmember of olivine (fayalite), wadsleyite and ringwoodite. Grey lines indicate maximum water content per mineral and the pink area shows the uncertainty ranges assigned to each parameter in our calculations. For references see Tables 2-4 in Appendix A.

range from $24.7{\cdot}10^{-6}$ to $40{\cdot}10^{-6}$ for ringwoodite (Smyth et al., 2003; Ye et al., 2009), 30e-6 for wadsleyite, and 38.1e-6 for olivine (Ye et al., 2009). The limited amount of experimental data prevented us from constraining γ, q_0 and η_0 as a function of water content. Instead we assumed the same property values as those defined at anhydrous conditions in Stixrude and Lithgow-Bertelloni (2011). Considering the uncertainties on our final models, this seems a reasonable assumption.

3.3.3 Helmholtz free energy and Debye temperature (F_0, θ_0)

Defining Helmholtz free energy (F_0) is particularly challenging because it is a theoretical parameter and cannot be measured directly by experiment. The Debye temperature, θ_0, can be measured experimentally but only limited data is available in literature for the hydrous NAMs. It is important to constrain these two parameters because they have a major effect on the position of the phase boundaries. Though all elastic parameters influence the phase boundary to some extent, F_0 is the key parameter for the shift of the phase boundary with respect to pressure, while θ_0 determines the Clapeyron slope (gradient between pressure and temperature, in Pa/K) of the phase boundary.

Theoretical values of F_0

The Helmholtz free energy is a relative parameter in the database of Stixrude and Lithgow-Bertelloni (2011). These relative values determine at what pressure and temperature each mineral is stable. This means that for any composition, the phase diagram will remain the same as long as the F_0 for each mineral involved is altered by the same amount. Theoretically, the Helmholtz free energy of a system can be calculated by the following formula:

$$F_0 = U - TS \tag{7}$$

where F_0 is the Helmholtz free energy (in J), U the internal energy (in J), T the absolute temperature (in K) and S the final entropy (in J/K). To constrain this property theoretically, it would be necessary to have the data of the latter three parameters for each NAM as a function of water content. As far as we could find in the literature up to 2014, this data is largely unavailable, so in this study we choose to derive the F_0 values from experimental observations of the phase boundary.

Theoretical values of θ_0

The Debye temperature can be described as the temperature of a crystal's highest normal mode of vibration (Hill, 2012). To increase the internal consistency of our models, we prefer to calculate the Debye temperatures from other mineral parameters instead of deriving them from experimental data. There are several methods to calculate the Debye temperature, these include calculation from (1) the elastic properties, (2) heat capacity or (3) vibrational entropy. Since we have already derived the elastic properties of the NAMs at hydrous conditions, our preference lies with the first method. We use the following formula to calculate the Debye temperature from elastic properties (from Anderson (1963)):

$$\Theta_D = 251.2(\frac{\rho}{\bar{M}})^{1/3}\bar{v} \tag{8}$$

where $\bar{v}$ is the Debye average sound velocity:

$$\bar{v} = \sqrt[3]{3}\left(\frac{1}{v_P^3} + \frac{2}{v_S^3}\right)^{-1/3} \tag{9}$$

with V_{P} and V_{S} the compressional and shear wavespeeds, given by Equation 1.

The second method that we investigated was to derive the Debye temperature from the heat capacity. The Debye temperature derived this way is called the calorimetric Debye temperature (θ_D), computed by the following formula (Blackman, 1955):

$$C_v \cong 234nNk_B \left(\frac{T}{\theta_D}\right)^3 \tag{10}$$

Where C_v is the heat capacity at constant volume, n the number of atoms per formula unit, N number of modes, k_B the Boltzmann constant and T the temperature (at C_v). This method, however, is only valid at low temperatures, where $T \ll \theta_D$ and C_v varies as T^3 (Debye's T^3 law). Therefore, heat capacities at low temperatures (and hydrous conditions) are needed per NAM to constrain the Debye temperature with this method.

The third way to calculate the Debye temperature is from the vibrational entropy, where the quasi-harmonic vibrational entropy per atom can be calculated by (Barron et al., 1957):

$$S = 3R\left\{\frac{4}{3} - ln\frac{\theta(0)}{T} + \frac{3B_2}{10\cdot 2!}\left[\frac{\theta(2)}{T}\right]^2 - \frac{9B_4}{28\cdot 4!}\left(\frac{\theta(4)}{T}\right]^4 + \dots\right\} \tag{11}$$

Where S is the vibrational entropy per atom, R the gas constant, θ_n the n^th moment of vibrational density states, T the temperature and B_n Bernoulli numbers. At higher temperatures (∼1000 K), only the first two terms are relevant and subsequent terms account for less than 1 percent of the total vibrational entropy. Rearranging 11 gives,

$$\theta(0) = T \cdot \exp\left(\frac{4}{3} - \frac{S}{3R}\right) \tag{12}$$

Very limited data are available for the vibrational entropy or heat capacity of the NAMs at hydrous conditions, so the second and third option could not be used to constrain the Debye temperature within realistic bounds.

We tested the validity of the first method by comparing the phase diagram computed from the anhydrous thermoelastic dataset of Stixrude and Lithgow-Bertelloni (2011) with a phase diagram computed from the same dataset, but with alternative Debye temperatures for all minerals calculated from their corresponding elastic properties. After redefining F_0 for the latter model, a clear distinction was found between the two phase diagrams, indicating that this method could not be used in this study. It is unclear why our Debye temperatures vary so much from the ones described in Stixrude and Lithgow-Bertelloni (2011), in some cases up to 15%. We compared our values of θ_0 to those published by Anderson (1963) and they were almost identical. We suggest that the θ_0 values published by Stixrude and Lithgow-Bertelloni (2011) may differ because the inversion procedure through which they were derived may cause them to be correlated with the F_0 values or other parameters.

Since all three methods described above could not be used due to either insufficient data or failing to pass the validity test, we ultimately decided to infer the Debye temperature indirectly from experimental data of the phase diagrams.

Experimental values of F_0 and θ_0

In order to determine F_0 and θ_0 from experimental data, we made a compilation of experimentally

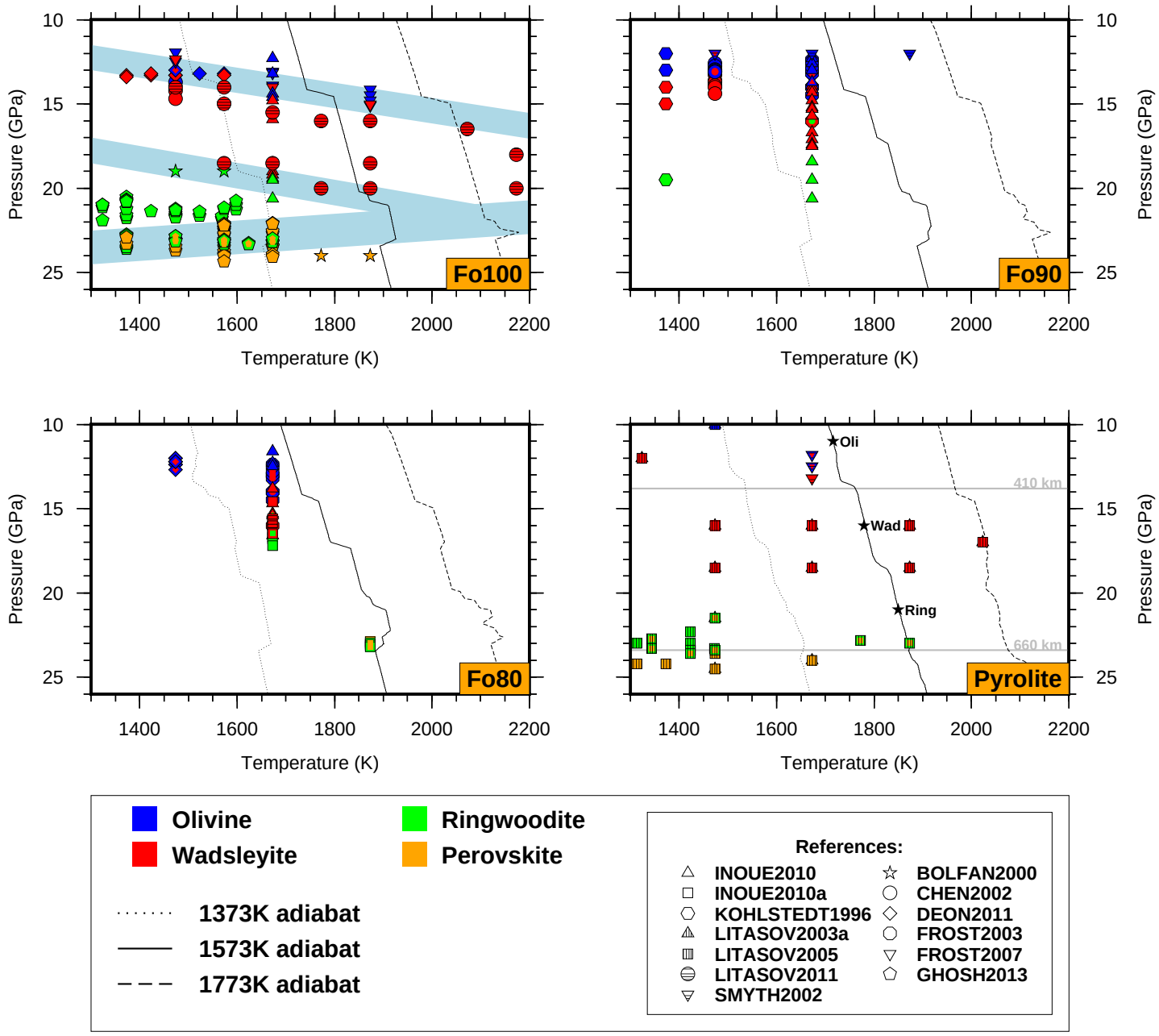

Figure 5: Experimental constraints on the phase boundaries between hydrous olivine, wadsleyite, ringwoodite and perovskite with different compositions. Adiabatic P-T paths are shown for potential temperatures of 1373 K (dotted line), 1573 K (solid line) and 1773 K (dashed line). Light blue bands in the pure Mg composition (top, left) indicate the range of possible phase boundaries that were used to derive the F_0 and θ_0 values for the Mg-endmember of each mineral. The black stars in the pyrolitic composition (bottom, right) indicate the median pressure and temperature of the phase between 300 and 800 km depth. These P-T points were used to determine the overall average water storage capacity for the phase (See Figure 1).

derived phase boundary points between olivine-wadsleyite, wadsleyite-ringwoodite and ringwoodite-perovskite, under hydrous conditions. Resulting P-T data points are plotted in Figure 5, for compositions of Fo100 (66.6 mol% MgO, 33.3 mol% SiO2), Fo90 (60 mol% MgO, 6.6 mol% FeO, 33.3 mol% SiO2), Fo80 (53.3 mol% MgO, 13.3 mol% FeO, 33.3 mol% SiO2) and pyrolite. The diagrams show that at low temperatures (up to 1673 K), the phase boundaries are reasonable well constrained, especially for the pure Mg (Fo100) composition. At higher temperatures, however, data is reduced to a few single data points. We extended phase boundaries to the P-T field of interest (i.e. expected pressure and temperature conditions in the mantle transition zone) by extrapolation, where all available experimental data points are contained within the upper and lower limit of possible phase boundary values.

To obtain values of F_0 and θ_0 for the Mg-endmember of each NAM, we used the Fe-free composition Fo100. For each of the 10 000 runs, we started with randomly chosen F_0 and θ_0 values. The F_0 and θ_0 were then updated iteratively, by adjusting F_0 to shift the phase boundary with respect to pressure, and θ_0 to change the Clapeyron slope until the boundary lay within the blue bands shown in Figure 5 (top left). A graphical overview of θ_0 and F_0 values that we obtained in this study is shown in Appendix B.

To our knowledge, no data is available for hydrous phase boundaries of a Mg-free composition (66.6 mol% FeO, 33.3 mol% SiO2). Some data on Mg-Fe mixed compositions could be found (Figure 5, top-right for $\frac{Fe}{Fe+Mg} = 10$, bottom-left for $\frac{Fe}{Fe+Mg} = 20$, in mol%), which we used to put a general constraint on the F_0 and θ_0 values of the Fe-endmember. Using the new F_0 and θ_0 values for the hydrous Mg endmembers and the F_0 and θ_0 values of the anhydrous Fe endmembers (from Stixrude and Lithgow-Bertelloni, 2011), we checked if the phase boundaries of the Mg/Fe mixed composition fell within the experimental data, which was generally the case. If not we altered the F_0 and θ_0 values of the endmembers until they did fit.

3.4 Density calculations for hydrous minerals

At anhydrous conditions, we assume that the bulk chemical composition is constant with depth (and temperature) and *Perple_x* can be used to directly calculate the density, V_s and V_P at any point within a 2D grid of P-T points. At hydrous conditions, however, this is not possible since each NAM has a different water storage capacity, and therefore it is likely that the amount of water stored within each mineral is different. Thus, we may have a variable bulk composition with depth, depending on the fraction of the hydrous phase and the wt% water inside that phase. At each P-T point, *Perple_x* computes the local density per mineral by dividing the molar mass by the local volume per formula unit. Since the incorporation of water changes the formula unit of a mineral, we have to recalculate the density of each hydrous mineral relative to its anhydrous counterpart. This can be done by computing the new molar mass of the hydrous minerals and dividing this by the volume per formula unit (as derived from ambient conditions by *Perple_X* using an EoS, see Section 2).

The molar mass of a hydrous phase depends on two criteria: (1) the wt% water of the phase and (2) how the H^+ atoms (protons) are incorporated within the atomic structure (type of protonation). There are three main types of protonation in NAMs. These are: substitution of Mg^{2+} vacancies ($Mg^{2+} \leftrightarrow 2H^+$), substitution of Si^{4+} vacancies ($Si^{4+} \leftrightarrow 4H^+$), or a combination of the two (Daniel et al., 2003; Mosenfelder et al., 2006; Litasov et al., 2007; Kohlstedt et al., 1996). In the case of

Mg-substitution, the resulting formula unit is $(Mg,Fe)_{2-x_1}SiO_4H_{2x_1}$, where x_1 is

$$x_1 = M_{anh}\left(\frac{2H^+ + O^{2-}}{W_f} + Mg^{2+} - 2H^+\right)^{-1} \tag{13}$$

or

$$x_1 = M_{anh}\left(22.3 + \frac{18.02}{W_f}\right)^{-1} \tag{14}$$

Where W_f is the water weight fraction, M_{anh} is the atomic weight of one formula unit at anhydrous conditions, and H^+, O^{2-}, Mg^{2+} are the atomic weights of H, O and Mg, respectively. Substituting (14) into the formula unit, we produce the following formula for the atomic weight at hydrous conditions (M_h), as a function of water weight fraction W_f:

$$M_h = M_{anh} \cdot (1 + 1.237W_f)^{-1} \tag{15}$$

Mg-substitution is thought to be the main mechanism behind H^+ storage in wadsleyite (Smyth, 1987; Jacobsen et al., 2005; Tian et al., 2012; Yang et al., 2014) and ringwoodite (51-66% according to Panero (2010), first principles study). In olivine, protonation of Mg-vacancies is the main mechanism at low pressure (Demouchy and Mackwell, 2006) but with increasing pressure Si-substitution becomes more important (Litasov et al., 2007).

In a similar way, we can compute the molar weight for Si-substitution $(Mg,Fe)_2Si_{1-x_2}O_4H_{4x_2}$, where

$$x_2 = M_{anh}\left(24.1 + \frac{36.0}{W_f}\right)^{-1} \tag{16}$$

and corresponding molar mass of

$$M_h = M_{anh} \cdot (1 + 0.668W_f)^{-1} \tag{17}$$

Si-substitution is the main protonation mechanism for hydrous olivine at high pressures. Also in ringwoodite, Si-substitution accounts for a significant part of H^+ storage, 24-41% according to Panero (2010).

Besides these primary mechanisms of protonation, one additional type has been found, where Si^{4+} is substituted by both H^+ and Mg^+ atoms ($Si^{4+} \leftrightarrow 2H^+ + Mg^{2+}$). This type of substitution has only been observed in ringwoodite, and may account for 8-10% of the total H^+ storage (Panero, 2010). The formula unit corresponding to this type of protonation is $(Mg,Fe)_{2+x_3}Si_{1-x_4}O_4H_{2x_3}$, where

$$x_3 = M_{anh}\left(1.76 + \frac{18.0}{W_f}\right)^{-1} \tag{18}$$

and molar mass,

$$M_h = M_{anh} \cdot (1 + 0.154W_f)^{-1} \tag{19}$$

Note that the three types of substitution all cause a decrease in the molar mass of the NAM. Combined with the effect of water on the volume (see Figure 3), which increases with increasing water content, we infer that the overall density goes down when water is present. A lower density would cause the velocity to be higher in hydrous minerals than in anhydrous minerals, if the bulk and shear moduli would remain constant or decrease at a lower rate than the density.

3.5 Test runs

To get a basic understanding of the effect of water on the elastic properties of the NAMs, we first investigate various stages of hydration of simple (Fe)-Mg-Si-O compositions, namely Fo100 and Fo90. These simple compositions reduce the number of stable minerals at transition zone conditions, and therefore amplify the influence of the NAMs on the seismic profile.

To estimate the effect of water on a more realistic mantle composition, we then investigate the hydration of a pyrolitic composition, with water content varying from anhydrous up to 3.3 wt% water. We compute two additional anhydrous models to compare our findings with other thermochemical effects: 1) anhydrous pyrolite with an increased iron content (+3 mol% FeO) and 2) anhydrous pyrolite with a 1773 K adiabat P-T path.

4 Results

4.1 Mg_2SiO_4 and $(Mg,Fe)_2SiO_4$ compositions

Synthetic seismic models for water contents of 0.0, 1.0, 2.0 and 3.3 wt%, along a 1573 K adiabatic P-T path in Fo100 and Fo90, are shown in Figure 6 and 7. Quantitative representations of the average density and velocities in the transition zone are plotted in Figures 8 and 9, and of the average gradients in Figures 10 and 11.

The results show that for the Fo100 and Fo90 compositions, water reduces the average density and velocities of the NAMs at transition zone conditions. The gradients, on the other hand, are elevated by the presence of water. The differences between anhydrous and hydrous compositions are larger for the Fo100 composition than for the Fo90 composition (particularly the gradients, Figures 10 and 11), indicating that the effect of water on the seismic properties of the NAMs decreases with increasing Fe content.

4.2 Pyrolitic composition

Figure 12 shows the computed density and velocity profiles between 300 and 900 km depth, for a pyrolitic composition with a 1573 K adiabatic P-T path at various water contents.

Despite their large uncertainties, the grey bands generally indicate a decrease in V_P and V_S in the transition zone with increasing water content. A 2-D graphical representation of the average velocities found in our models is shown in Figure 13 for the whole transition zone and Figure 14 for the interval between 450-600 km. The average V_P, V_S and density over these intervals are quantified in Figures 15 and 16. The average velocity gradients of the transition zone and 450-600 km interval are plotted as 2-D scatter diagrams in Figures 17 and 18, and as 1-D histograms in Figures 19 and 20.

4.2.1 Discontinuity depths

The depths of the '410' and '660' discontinuities (see Figure 12) show a larger uncertainty range for the anhydrous composition (402(24) km and 658(18) km, respectively, where the number in brackets is one standard deviation) than for the hydrous compositions (407(8) km and 629(9) km). In both

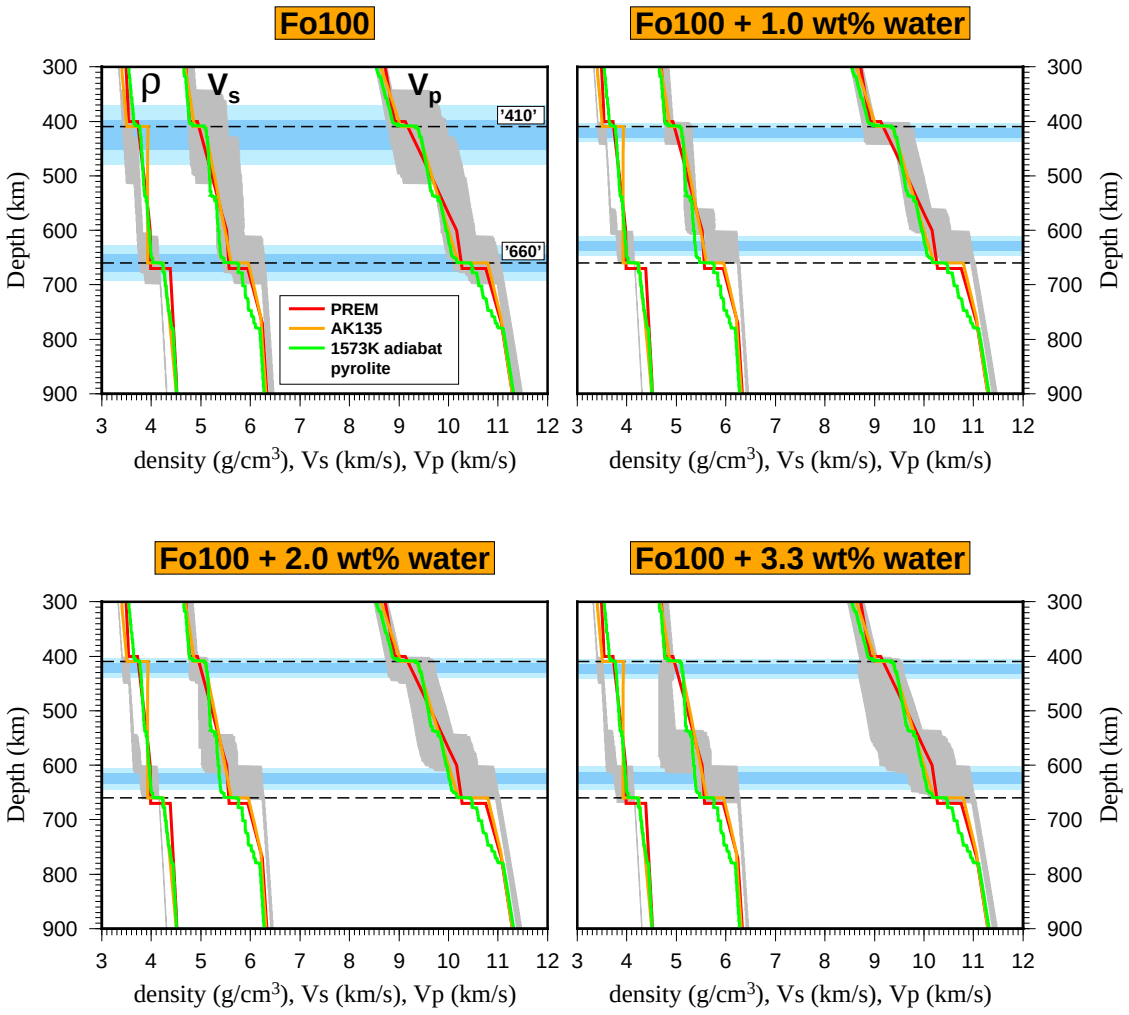

Figure 6: Density and velocity profiles through the mantle between 300 and 900 km, for the Fo100 bulk chemical composition. Shaded area shows the range of the 10 000 runs. Red, orange and green lines indicate PREM, AK135 and a typical 1573 K adiabatic pyrolite (anhydrous) profile computed from the dataset of Stixrude and Lithgow-Bertelloni (2011), respectively.

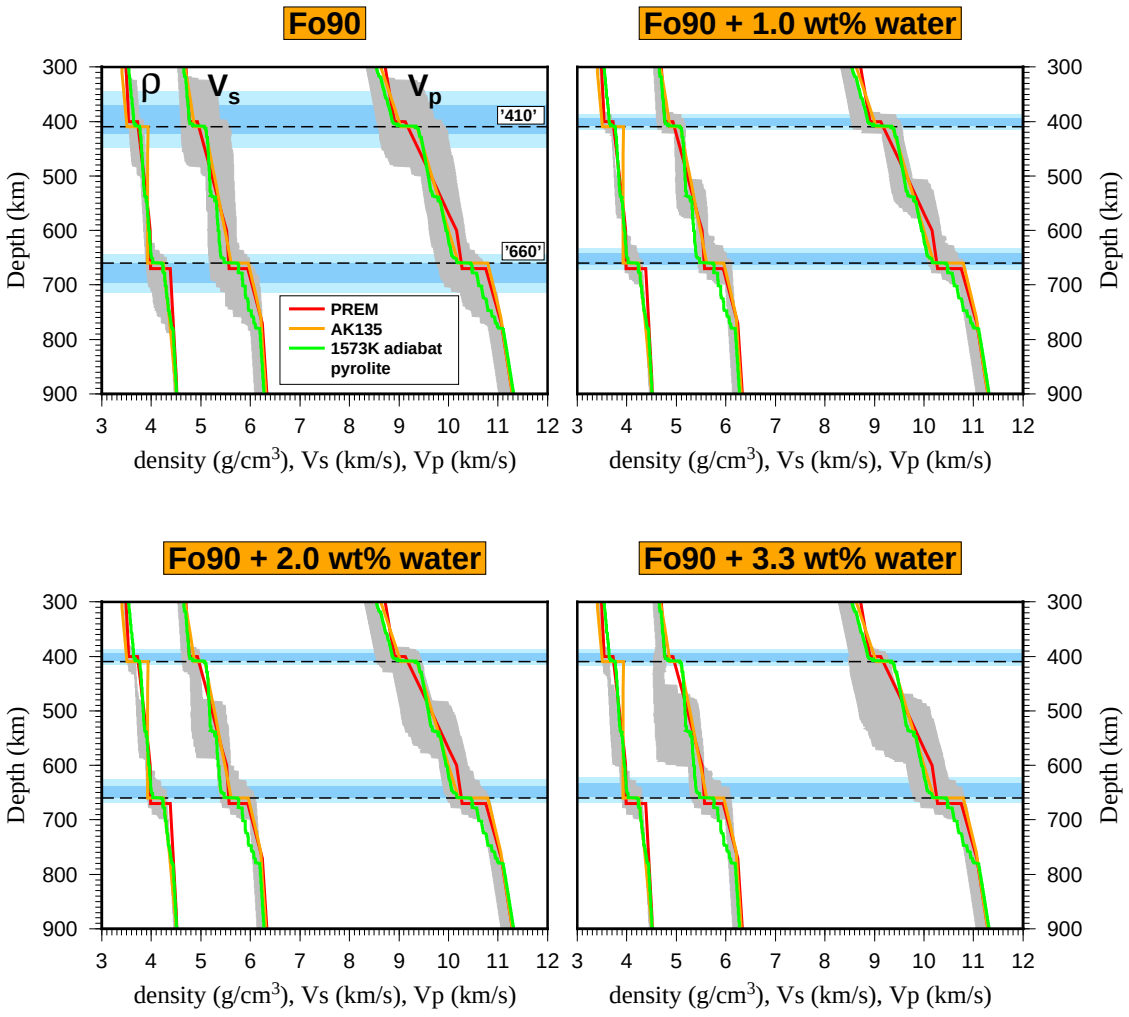

Figure 7: Density and velocity profiles for a Fo90 composition, for symbols and colour scheme see Figure 6.

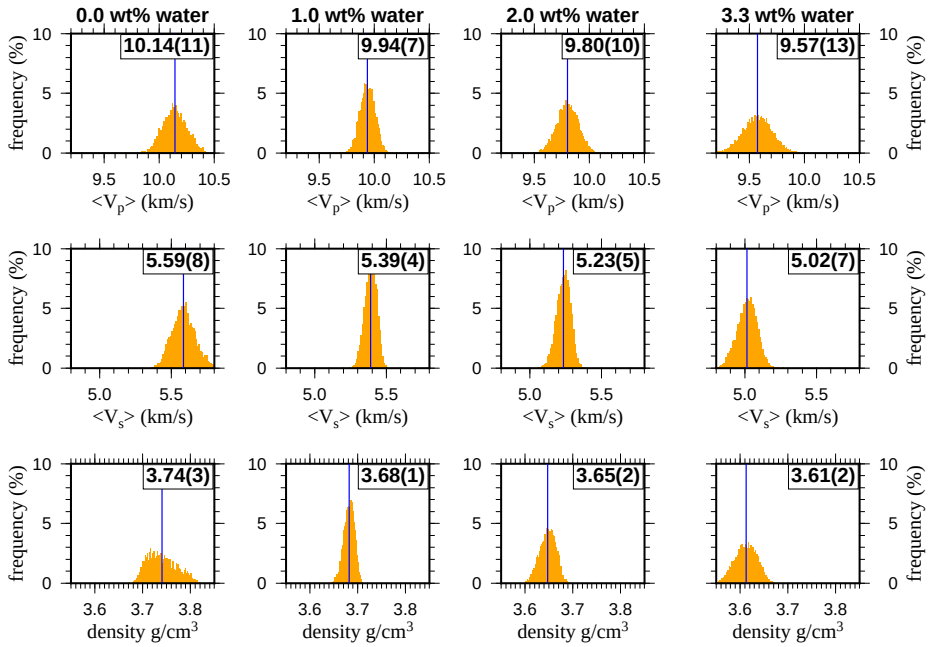

Figure 8: Average velocities and density of the transition zone for water contents of 0.0-3.3 wt% water and a Fo100 composition. Mean values, with one standard deviation in brackets, are given in the top right corner of each histogram and plotted as a blue line. The plots show a significant decrease in average velocities and density with increasing water content.

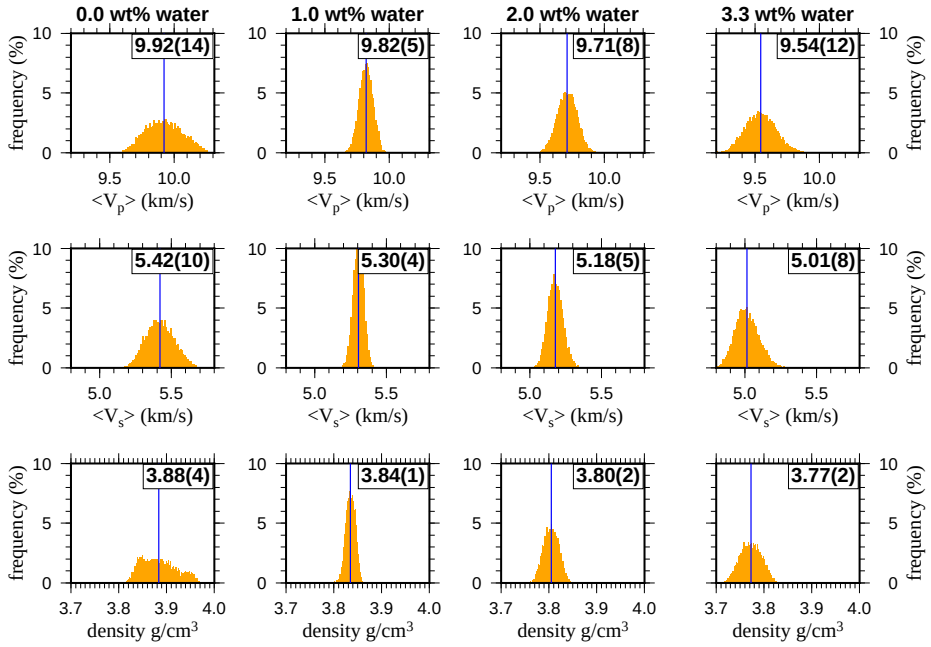

Figure 9: Average velocities and density of the transition zone for a Fo90 composition and varying water content. The decrease in all three with increasing water content is smaller than those found for the Fo100 composition, but still significant.

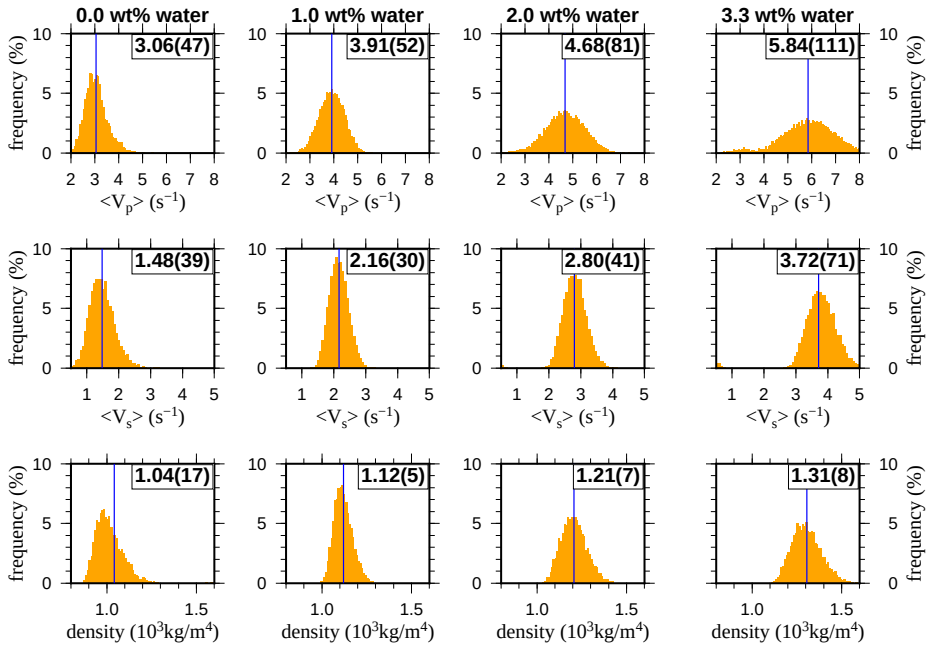

Figure 10: Average velocity and density gradients of the models described in Figure 6, between the '410' and '660' discontinuity. The gradients show an increase with increasing water content, up to double the mean value found for the anhydrous model.

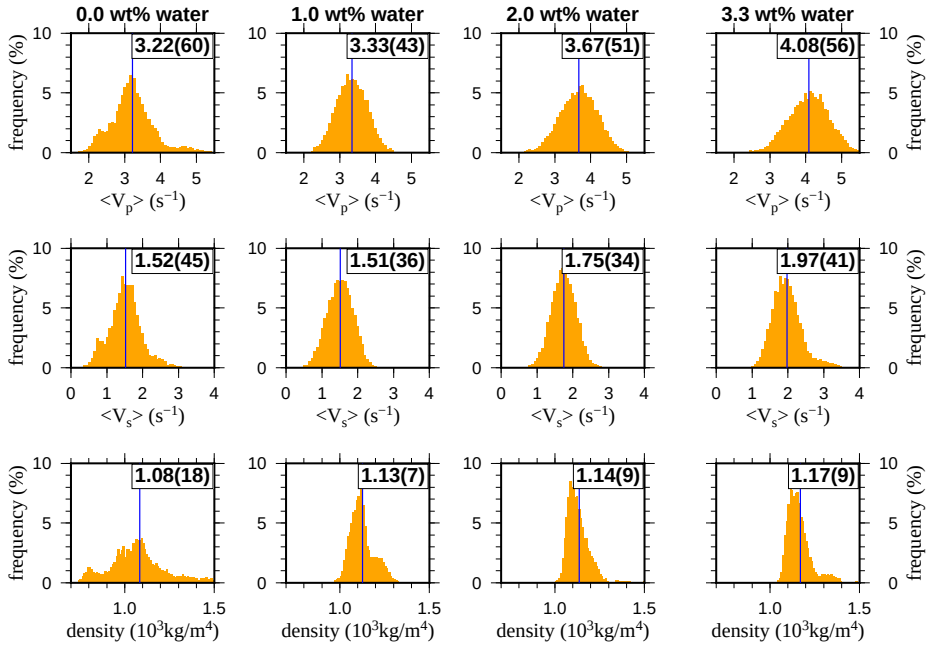

Figure 11: Average velocity and density gradients of the models described in Figure 7, between the '410' and '660' discontinuity. Compared to the gradients found for the Fo100 composition, the gradients of the Fo90 composition are smaller, but still clearly increase with increasing water content.

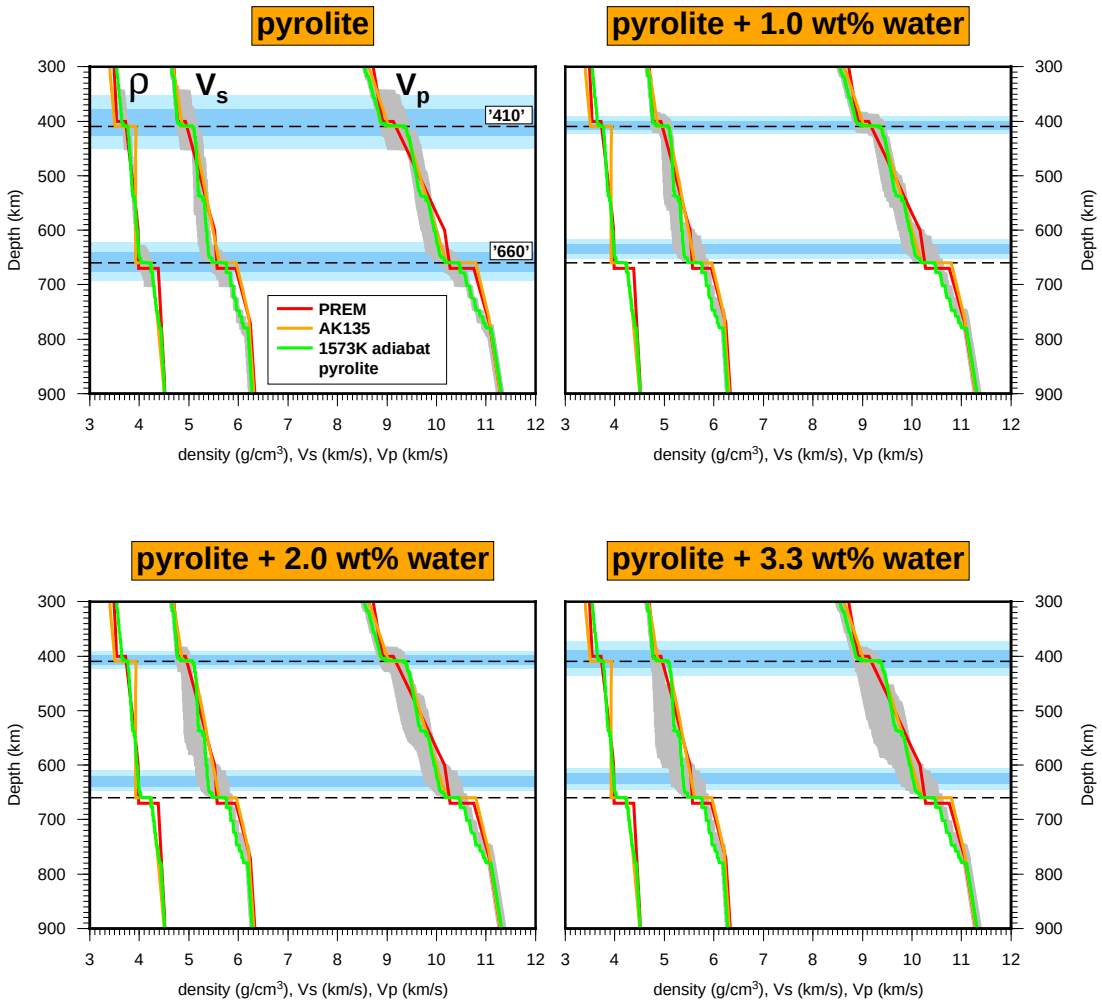

Figure 12: Density and velocity profiles through the mantle between 300 and 900 km for hydrous pyrolite. The ranges spanned by the 10 000 runs are plotted as grey bands. A typical 1573 K adiabatic mantle profile at anhydrous condition, based on the dataset of Stixrude and Lithgow-Bertelloni (2011), is plotted in green. The 1-D seismic reference models PREM and AK135 are also shown for comparison. Blue areas indicate the depth of the '410' and '660' discontinuities, at one standard deviation 1σ (dark blue), and 2σ (light blue).

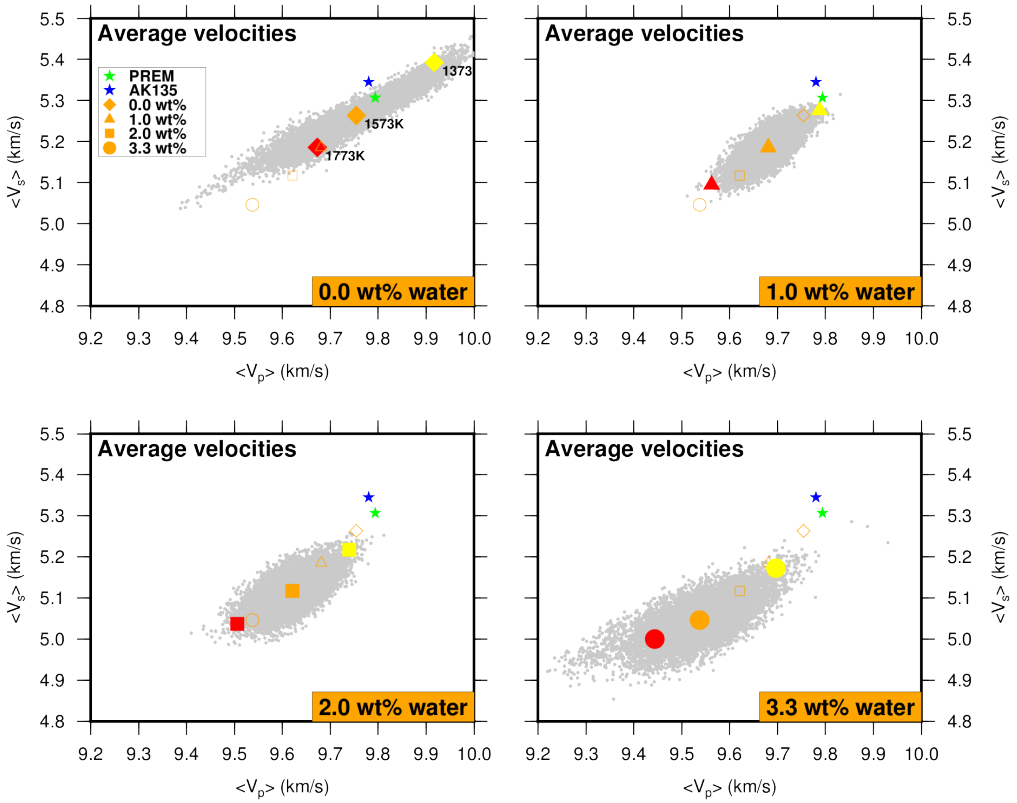

Figure 13: Average V_P and V_S of the mantle transition zone for a 1573 K adiabatic pyrolite composition and water contents 0.0-3.3 wt%. Individual runs are plotted in grey, with the mean value per water content in solid orange. Hollow symbols show mean values of the other plots for comparison. Yellow and red symbols indicate mean values for the colder (1373 K) and hotter (1773 K) adiabats, respectively. Seismic references PREM and AK135 are indicated by the green and blue symbols.

anhydrous and hydrous models, only the elastic parameters of the NAMs are changed, so the larger uncertainty range of the anhydrous models is caused by the larger uncertainty on F_0 and θ_0 of the NAMs for the anhydrous models. Only for the case of 3.3 wt% water does the standard deviation of the depth of the '410' discontinuity increase to 14 km. This is due to the small change in V_P, V_S and density at the '410', which in some models results in an absent or misinterpreted depth of the '410' discontinuity. The range of '410' discontinuity depths in the hydrous models fall well within 2σ of the anhydrous models, indicating that the effect of water on the shift of the '410' discontinuity cannot be resolved within the uncertainties of our models. The '660' discontinuity, on the other hand, is clearly shallower in the hydrous models than in the anhydrous models. Overlapping discontinuity depths are only present outside 1σ of the mean value. None of the hydrous models have a '660' discontinuity at 660km depth.

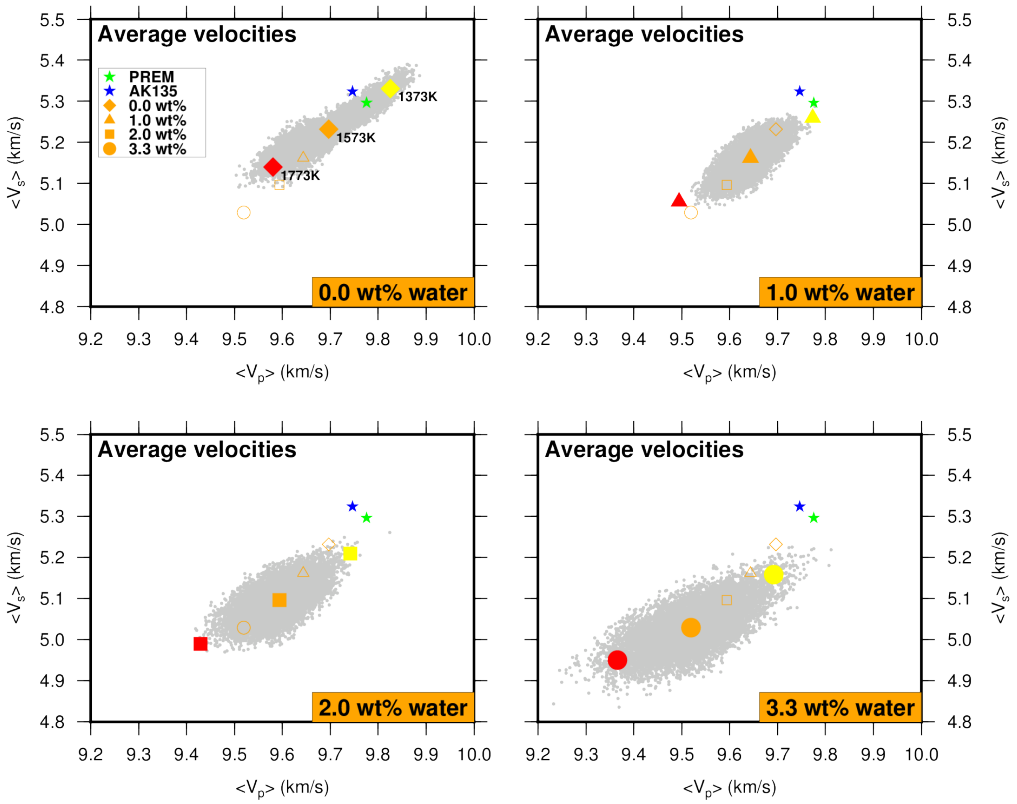

Figure 14: Average V_{P} and V_{S} for a pyrolitic composition over the interval 450-600 km. For colour and symbol description see Figure 13.

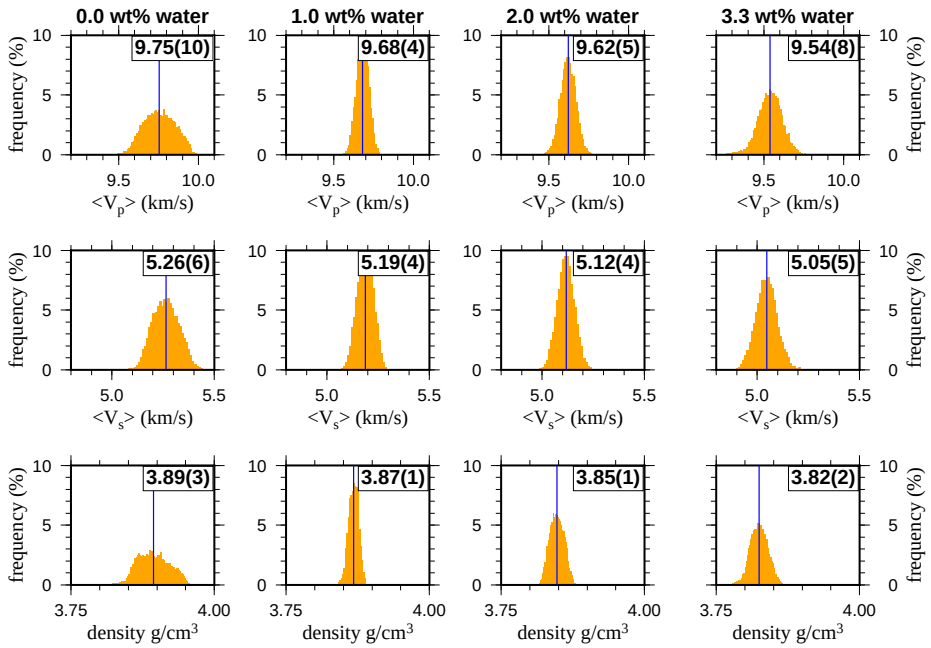

Figure 15: Average V_P, V_S and density of the transition zone, for a 1573 K adiabat P-T path in pyrolite and water content up to 3.3 wt%. Mean values are given in the top right of each histogram with 1σ between brackets, and indicated in the histograms by a blue line. V_P, V_S and density all display a decrease with increasing water content.

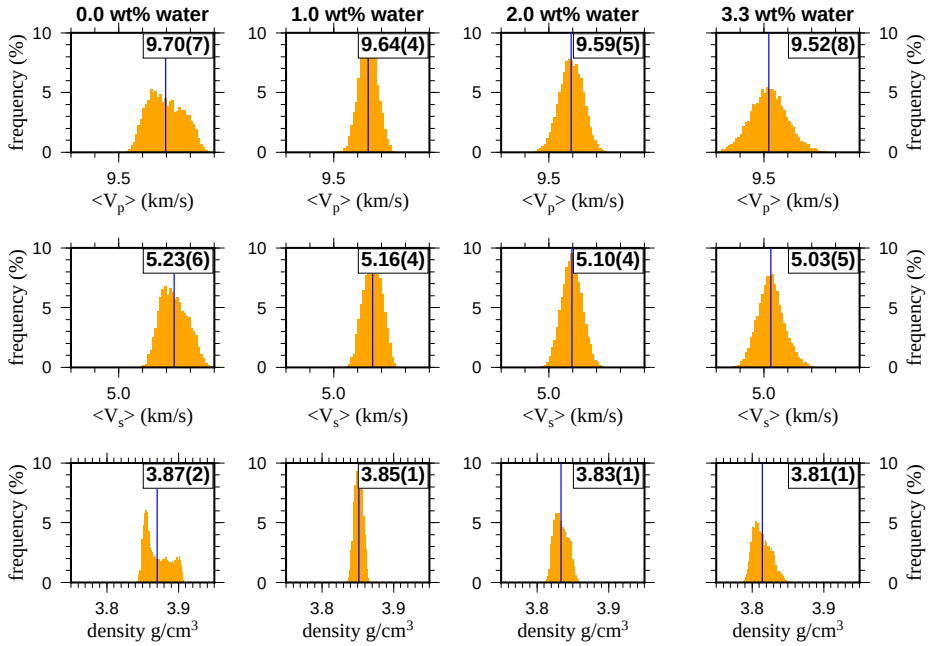

Figure 16: Average V_P, V_S and density of the interval 450-600 km, for 1573 K adiabatic pyrolite and water content up to 3.3 wt%. Mean V_P and V_S values lie within 1σ of the mean values plotted in Figure 15, indicating that variation in the depth of the phase boundaries has little effect on the average velocities in our models. Average density values also show little change compared to those of the whole transition zone.

4.2.2 Average velocities

The average V_P and V_S in the mantle transition zone (Figures 13 and 15) clearly show that average velocities (both V_P and V_S) decrease with increasing water content. At anhydrous conditions, the mean velocities are 9.75(10) kms^{-1} and 5.26(6) kms^{-1} for V_P and V_S respectively, decreasing to a minimum mean value of 9.54(8) kms^{-1} and 5.05(5) kms^{-1} at 3.3 wt% water. This yields a decrease of approximately -0.7 % per wt% water for V_P and -1.2 % per wt% water for V_S. The data also show a greater dispersion with increasing water content, which coincides with the larger uncertainties on mineral elastic properties with increasing water content (Figure 3). Mean values of the hotter and colder adiabats indicate that water does not change the temperature effect significantly. This is not surprising since we used the same temperature derivatives of K and G (i.e. γ_0, η_0 and q_0) for the hydrous models as for the anhydrous ones (Section 3.3.2). We also note that V_P and V_S decrease along nearly the same trend for an increase in temperature as for an increase in water content.

The position of the discontinuities might influence the average velocities. Each NAM displays a velocity increase with increasing depth, so a downward shift (depression) of either the '410' or '660' discontinuity is expected to result in an increase of the average velocity inside the mantle transition zone, and vice versa. For this reason, we also computed the average velocities at a depth interval between 450-600 km, following Cobden et al. (2008). This interval falls outside the 95 % confidence range of either discontinuity, and therefore influences of phase transitions associated with the discontinuities are small. The results (Figures 14 and 16) show the same trends as for the whole transition zone. From anhydrous to 3.3 wt% water, the mean V_P and V_S decrease from 9.70(7) kms^{-1} and 5.23(6) kms^{-1} to 9.52(8) kms^{-1} and 5.03(5) kms^{-1} respectively. Comparing 15 and 16 shows that the depths of the discontinuities do not appear to influence the average velocities significantly.

4.2.3 Average velocity gradients

The average velocity gradients in the transition zone, plotted in Figures 17 and 19, show that water increases the average gradients. At anhydrous conditions, the mean V_P and V_S gradients were found to be $3.22(60)\cdot10^{-3}$ s^{-1} and $1.52(45)\cdot10^{-3}$ s^{-1} respectively. These values increase to $4.08(56)\cdot10^{-3}$ s^{-1} and $1.97(41)\cdot10^{-3}$ s^{-1} at maximum water content (3.3 wt%), corresponding to an increase per wt% water of 8 % for V_P and 9 % V_S. Note that the mean value of the 1773 K adiabat in the 2.0 wt% and 3.3 wt% water compositions (Figure 17 bottom left, bottom right) does not lie on a straight line with the mean values of the 1373 K and 1573 K adiabats, which suggests that water influences the temperature effect on the velocity gradients.

However, this could also be due to the effect of the discontinuities, so in order to minimize discontinuity effects we again computed the average velocity gradients between 450 and 600 km depth (Figures 18 and 20). This interval shows the same general trend of increasing gradients with increasing water content, but the apparent change in temperature effect at high water contents has disappeared.

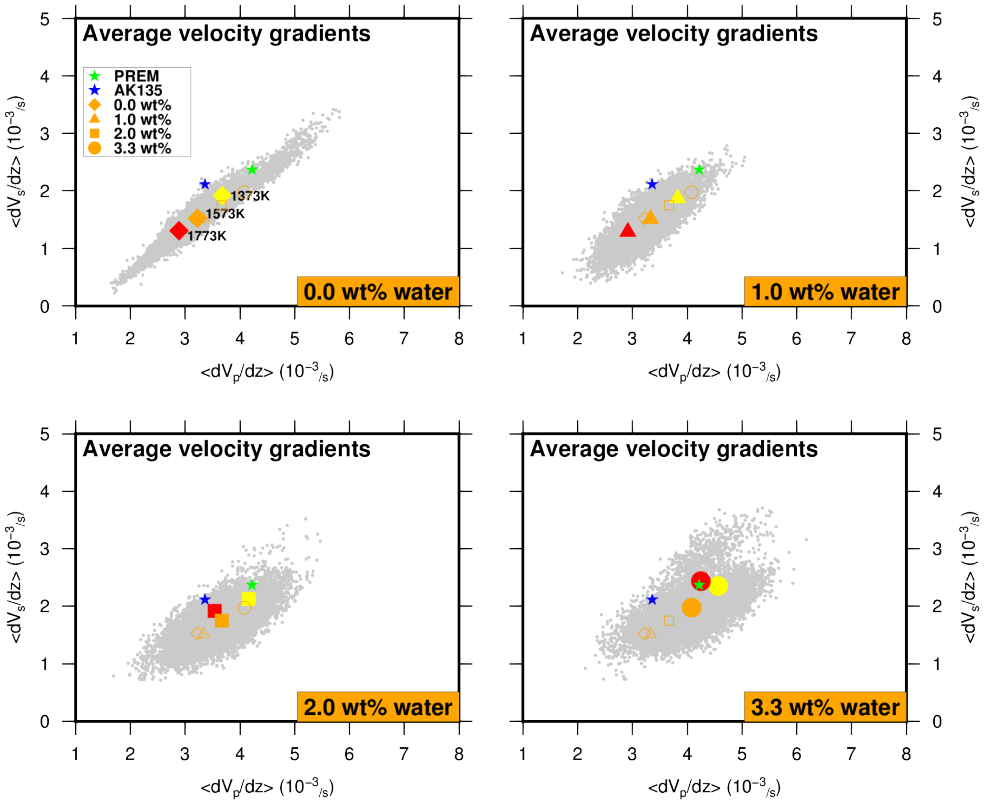

Figure 17: Average V_P and V_S gradients of the mantle transition zone for different amounts of water. See Figure 13 for symbol and colour description. The plots show an increasing gradient with water content for both V_P and V_S. The effect of water on the temperature dependence of the gradients is not constant from 1.0 wt% to 2.0 wt% to 3.3 wt%. This, however, could be due to the effect of the phase boundaries (See Discussion, Section 5.1).

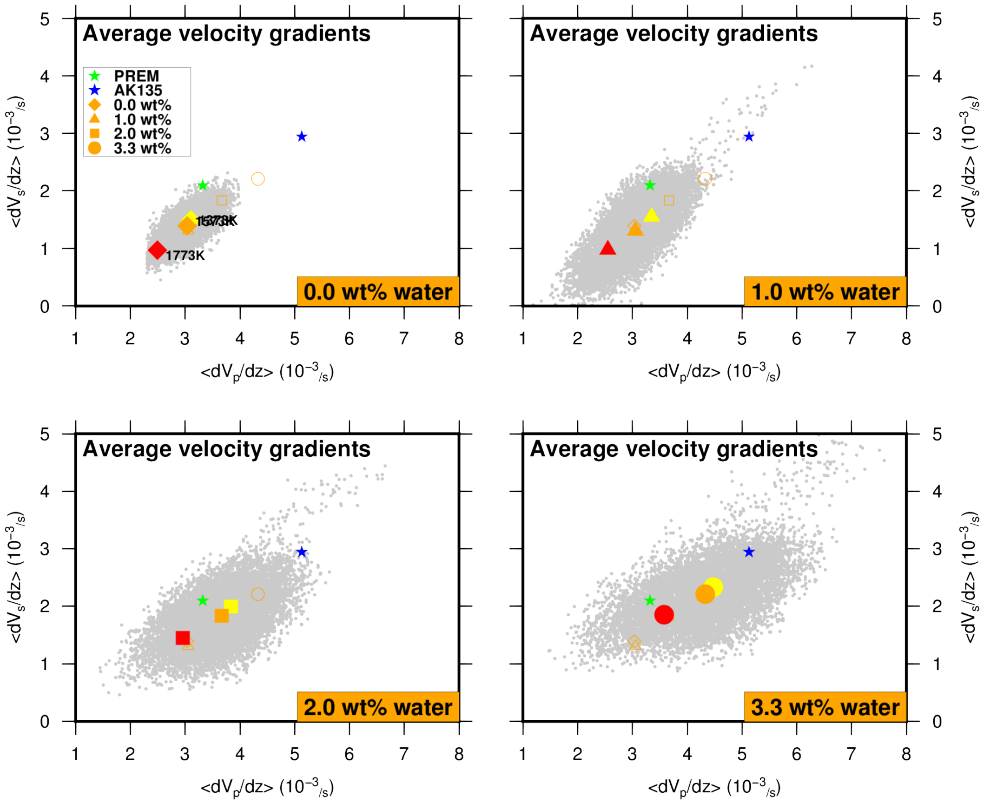

Figure 18: Average V_P and V_S gradients over the 450-600 km interval for models shown in Figure 17. The gradients of V_P and V_S both increase with increasing water content, which agrees with the results found for the whole transition zone. The variable temperature dependence with increasing water content found for the whole transition (see Figure 17) zone is significantly less pronounced at this depth interval.

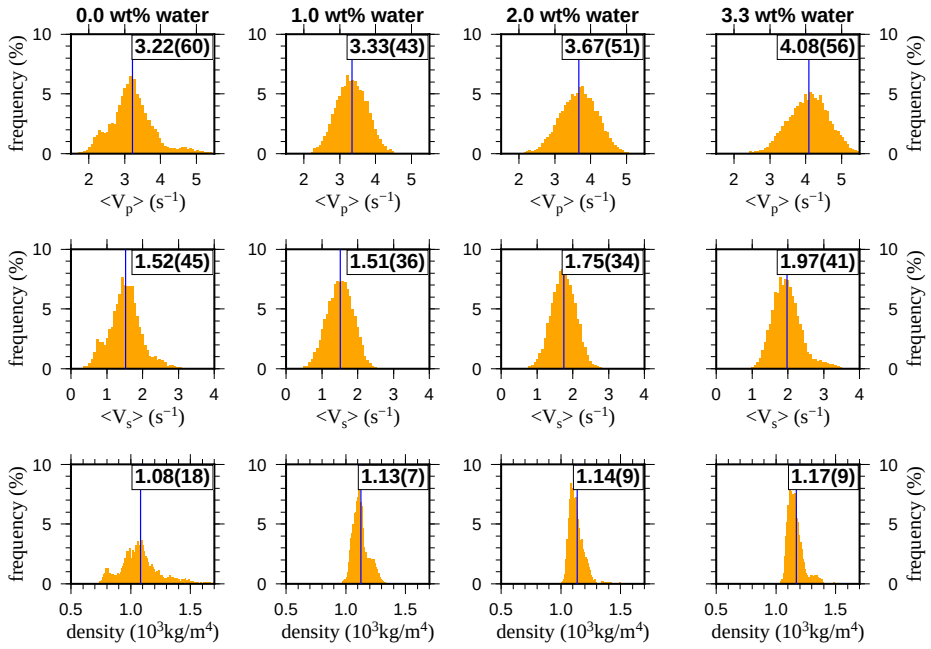

Figure 19: Results of the average V_P, V_S and density gradients in the transition zone, for a pyrolitic composition along a 1573 K adiabat. Mean and standard deviation values are plotted in the top right corner of each histogram. Average V_P and V_S gradients increase with increasing water content. The average density gradient increases only slightly, but within the range of the anhydrous composition.

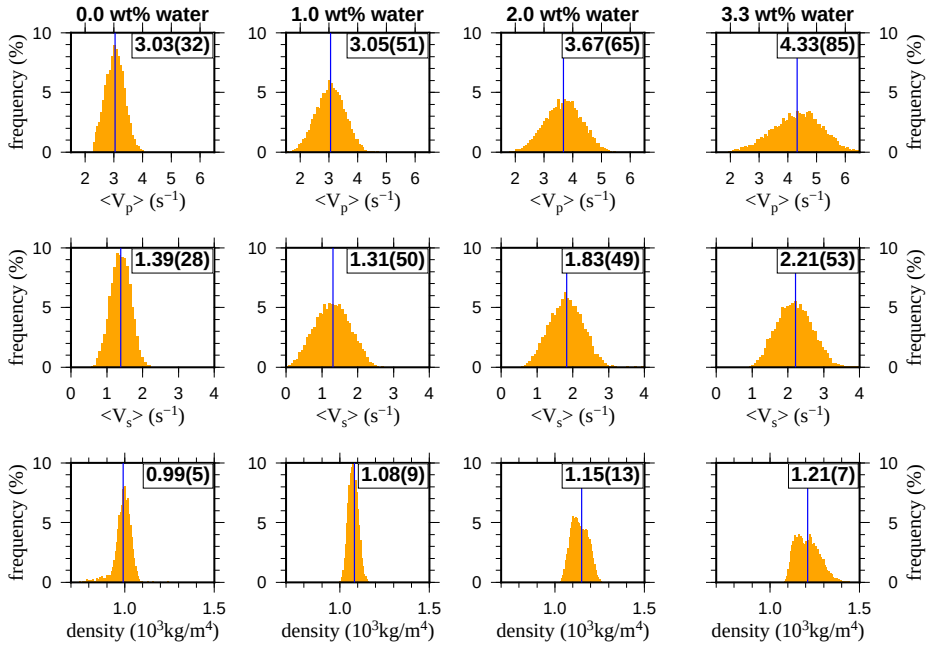

Figure 20: Average V_P, V_S and density gradients between 450 and 600 km, for a pyrolitic composition along a 1573 K adiabat. The distribution is closer to Gaussian than for the whole transition zone (Figure 19), but uncertainties are larger.

4.2.4 Impedance contrast

'410' discontinuity Figure 21 shows the V_P, V_S and density jump at the '410' discontinuity. The plots show a general decrease in all three of V_P, V_S and density jump at the '410' with increasing water content. At 3.3 wt% water, the jump in V_P decreases to values around zero. Since we determine the position of the '410' discontinuity primarily from the maximum jump in V_P, no '410' discontinuity could be determined for runs with V_P jump values very close to zero. The jump in V_S could not be used to constrain the '410' discontinuity because these values are also very close to zero. This is also evident from the velocity profile at 3.3 wt% shown in Figure 12 (bottom right). Considering the large uncertainties of the jumps compared to the small differences between the mean values of the 1373 K, 1573 K and 1773 K adiabats, water has no significant effect on the temperature dependence of the velocity and density changes at the '410' discontinuity. Important to note here, however, is that we assumed constant values for the temperature derivatives of K and G so we did not expect to see a significant temperature effect here. Changing the temperature derivatives might result in a more significant effect of water on the temperature dependence of the '410' discontinuity.

'660' discontinuity The V_P, V_S and density jumps at the '660' discontinuity are shown in Figure 22. Compared to the data of the '410' discontinuity, the data points at the '660' show a larger dispersion. No clear correlation was found between water content and change in V_P, V_S or density at the lower boundary of the transition zone.

A summary of the '410' and '660' impedance contrasts is given in Table 1, with some seismic observations for comparison. At the '410' discontinuity, both P and S impedance contrast for the synthetic models show much lower values than those found in seismic observations. The '660' discontinuity shows a better correlation with the seismic observations.

4.3 Changes in thermal structure and composition

To investigate whether it is possible to distinguish the effect of water on the transition zone structure from other thermochemical effects, we also computed 10 000 model to understand the effect of 1) changing the Fe content of the bulk composition and 2) a different thermal structure, at anhydrous conditions. The resulting profiles are shown in Figure 23, for anhydrous pyrolite (top-left), pyrolite with 1.5wt% water (top-right), pyrolite with increased water content (bottom-left) and pyrolite with 200 degrees higher temperature (bottom-right). It is evident from the plots that both a higher concentration of Fe and a hotter adiabat result in lower velocities in the transition zone. Quantifying the results (see Figure 24 and 25), we see that the decrease of the average velocity (compared to the reference anhydrous model) in the transition zone is of the same order of magnitude in each model. For Vp, the decrease is approximately 1 % for 1.5 wt% water, +3 mol% FeO or +200 K, which comes down to a decrease of ∼0.6 % per water weight percent, ∼0.2 % per mole FeO or ∼0.4 % per 100 K. The corresponding decreases in V_S are ∼1.4 %, ∼0.3 % and ∼0.7 %, respectively. The higher Fe content produces a different effect on the density than the other models, but it is not possible to distinguish between a hotter adiabat and an increased water content on the basis of Vp, V_S and density alone. Average values of the velocities and density in the transition zone are therefore not sufficient to make a clear distinction between temperature and water effects, although when combined they may be useful for identifying changes in iron content.

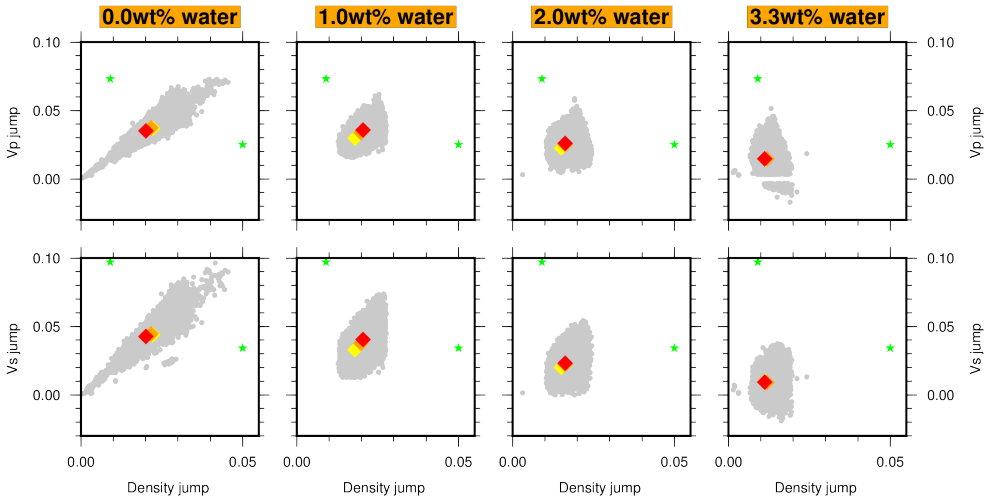

Figure 21: The fractional change in V_P, V_S and density at the '410' discontinuity, along a 1573 K adiabatic P-T path in a pyrolite composition. Data plotted in grey show 10 000 models for the 1573 K adiabat. Yellow, orange and red diamonds correspond to the mean values of the 1373 K, 1573 K and 1773 K adiabats, respectively. Green stars indicate seismic observations, from Shearer and Flanagan (1999) and Dziewonski and Anderson (1981).

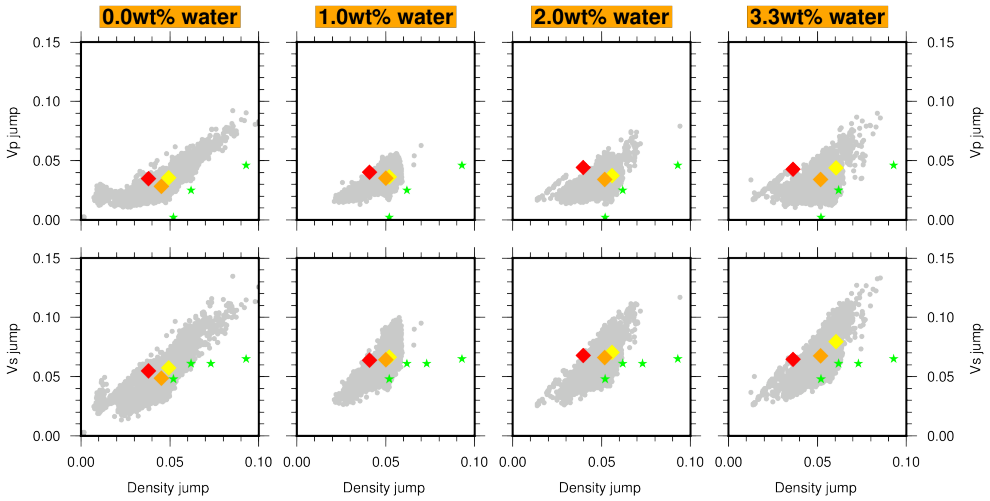

Figure 22: Fractional changes in V_P, V_S and density at the '660' discontinuity. Symbols are explained in Figure 21. Data shown as green stars are seismic observations from Shearer and Flanagan (1999); Dziewonski and Anderson (1981); Estabrook and Kind (1996); Revenaugh and Jordan (1991); Castle and Creager (2000); Kennett et al. (1995).

'410'		'660'				
P	S	P	S	data type	study area	reference
5.9(23)	6.6(26)	7.4(18)	9.4(22)	synthetic	0.0 wt% water	*this study*
5.6(27)	6.4(31)	7.1(21)	9.0(26)	synthetic	0.0 wt% water[a]	*this study*
5.4(10)	5.7(13)	8.5(8)	11.4(13)	synthetic	1.0 wt% water	*this study*
4.7(10)	4.8(12)	8.6(9)	11.6(14)	synthetic	1.5 wt% water	*this study*
4.1(9)	3.9(11)	8.6(10)	11.8(15)	synthetic	2.0 wt% water	*this study*
2.6(9)	2.1(10)	8.6(16)	11.9(22)	synthetic	3.3 wt% water	*this study*
5.4(23)	6.0(26)	7.2(18)	9.1(22)	synthetic	3.0 mol% Fe	*this study*
7.5	8.4	13.9	15.8	P and S, various	Global (PREM model)	Dziewonski and Anderson (1981)[b]
15.01	15.65	12.93	13.4	P and S, various	Global (Ak135 model)	Kennett et al. (1995)[b]
8.2	10.6	7.2	10.0	PP & SS precursors	Global	Shearer and Flanagan (1999)
	4.6(10)		14.4(20)	ScS	Indo-australia, West Pacific	Revenaugh and Jordan (1991)
	6.7(11)		9.9(15)	P & SH multiples, SS precursors, P-to-SV conv. phases	Global	Shearer (1991)
7.6		7.2		P'P' precursors	S Atlantic Ocean, Indian Ocean, Antartica	Xu et al. (2003)
4.6(10)	9.5(27)			PP & SS precursors	Asia (NE)	Chambers et al. (2005b)
6.4(15)	7.9(19)			PP & SS precursors	Pacific (NW)	Chambers et al. (2005b)
8.7(20)	7.7(24)			PP & SS precursors	Pacific (NE)	Chambers et al. (2005b)
5.1(13)	7.2(19)			PP & SS precursors	North America	Chambers et al. (2005b)
5.3(3)	7.8(6)			PP & SS precursors	Combined	Chambers et al. (2005b)
	6.7(11)		9.9(15)	SS precursors	Global	Shearer (1996)
6.5				PP precursors	Central & Northern Pacific	Rost and Weber (2002)
		8.7	12.30	PP precursors	Global	Estabrook and Kind (1996)

Table 1: Impedance contrast (in %) from this study compared to seismic observations. *a* - 1773K adiabat, *b* - Impedance contrast derived from 1-D reference models.

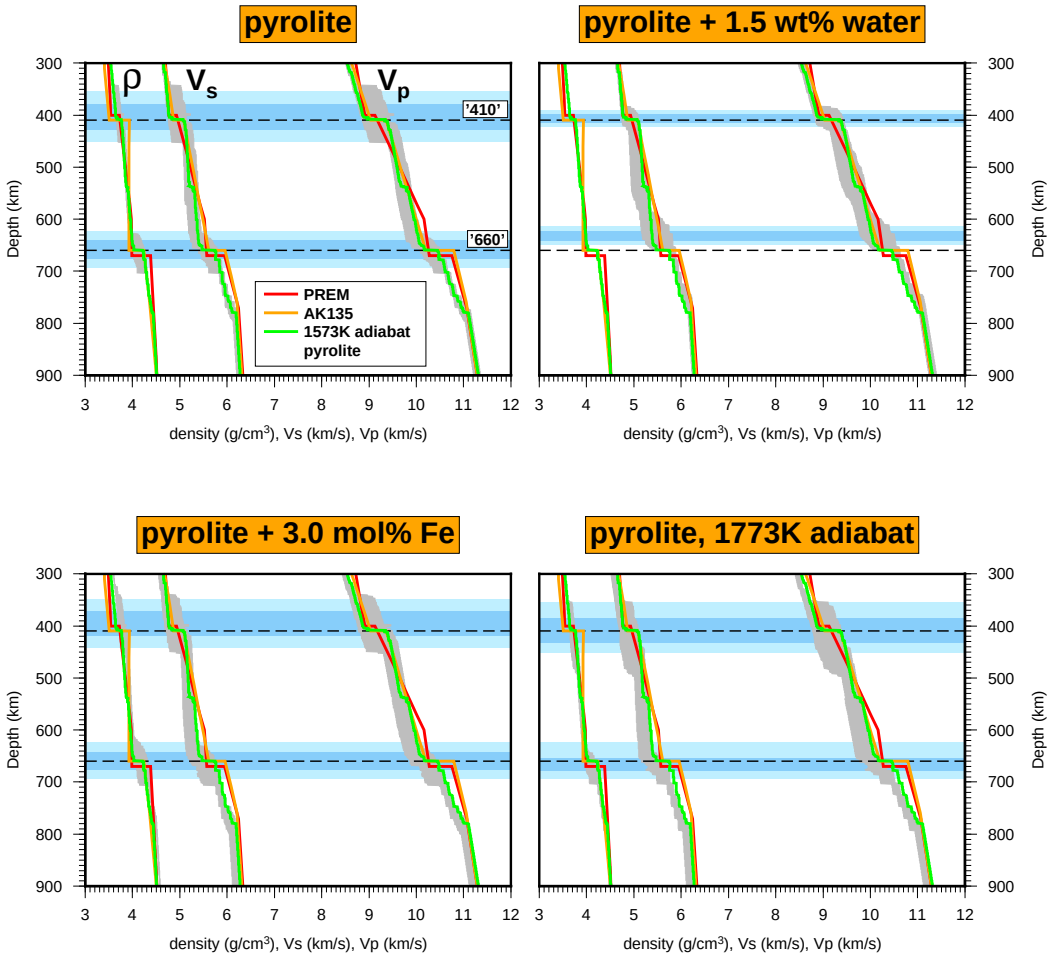

Figure 23: Density and velocity profiles for an anhydrous (top left), hydrous (top right) and increased Fe content (bottom left) pyrolite composition along a 1573 K adiabat, and an anhydrous pyrolitic composition along a 1773 K adiabat P-T path (bottom right). Grey bands indicate ranges spanned by 10 000 models.

However, comparing the average velocity gradients in the transition zone, we find that increasing the Fe content does not affect the velocity gradients in the transition zone and a higher temperature decreases the average gradients. This in contrast to the hydrous model, where the average velocity gradients increase. 1.5wt% water increases the average velocity gradients significantly (up to 15% for the V_S gradient).

Changes in thermal structure or composition have little effect on the impedance contrast of both discontinuities (Figures 26 and 27) and Table 1). A higher Fe content or hotter adiabat result in smaller P and S impedance contrasts at both discontinuities, but these changes are small compared to the large uncertainties on the impedance contrasts at anhydrous conditions. This implies that a distinction can be made between chemical/temperature effects and water presence based on the impedance contrast, since water does have an effect on the impedance contrast. Considering, however, the small differences between the mean values of the models compared to the large uncertainties (Figures 26 and 27, it is unclear if this distinction could actually be made in real seismic observations.

4.4 Summary

Summarizing the main results of our models, we find that:

1. Water decreases the average V_P, V_S and density of the transition zone by ∼0.7 %, ∼1.2 % and ∼0.5 %, respectively, per wt% water.
2. The velocity gradients increase significantly with increasing water content, with about ∼8 % for Vp, ∼9 % for Vs, and ∼4 % for density, per wt% water.
3. It is possible to make a distinction between changes in Fe content and changes in water content based on the average velocity and density of the transition zone alone, but not between changes in water content and the thermal structure.
4. The velocity gradients are much more affected by water than by changes in Fe content or thermal structure, so the gradients may be useful for distinguishing water from other thermalchemical effects.
5. The P and S impedance contrasts at the '410' discontinuity decrease with increasing water content, from 5.9(23) and 6.6(26) at anhydrous conditions to a minimum of 2.6(9) and 2.1(10) at 3.3 wt%. The impedance contrasts of the alternative thermochemical models also show a decrease with respect to those at anhydrous conditions, but these changes are very small compared to the uncertainties.
6. No clear relationship was found between water content and the change in impedance contrast at the '660' discontinuity.

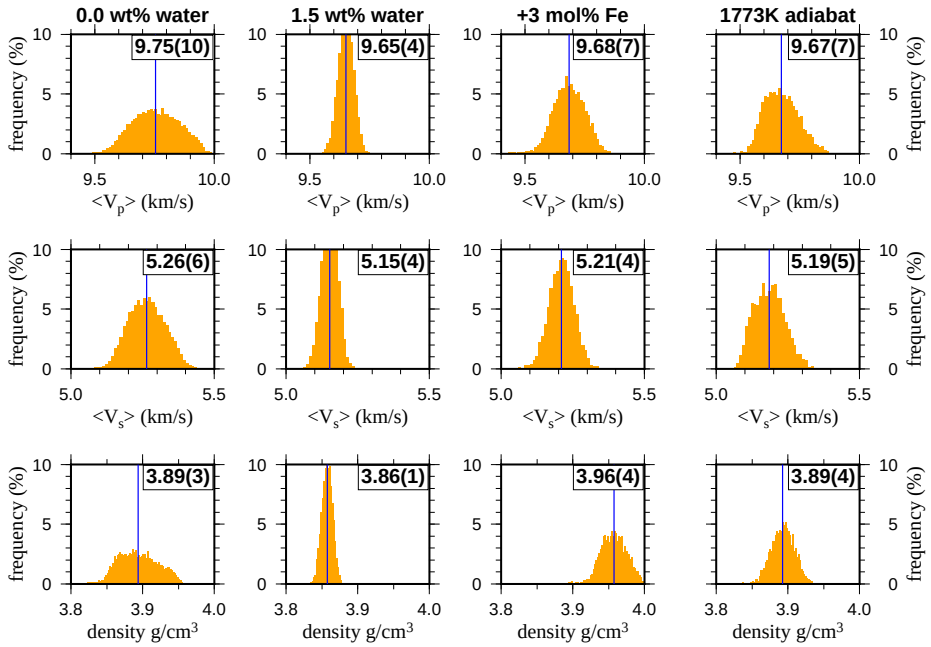

Figure 24: Average V_P, V_S and density of the transition zone, for anhydrous pyrolite (top-left), pyrolite with 1.5 wt% water (top-right), pyrolite plus 3.0 mol% Fe (bottom-left) and anhydrous pyrolite at higher temperature (+200 K, bottom-right).

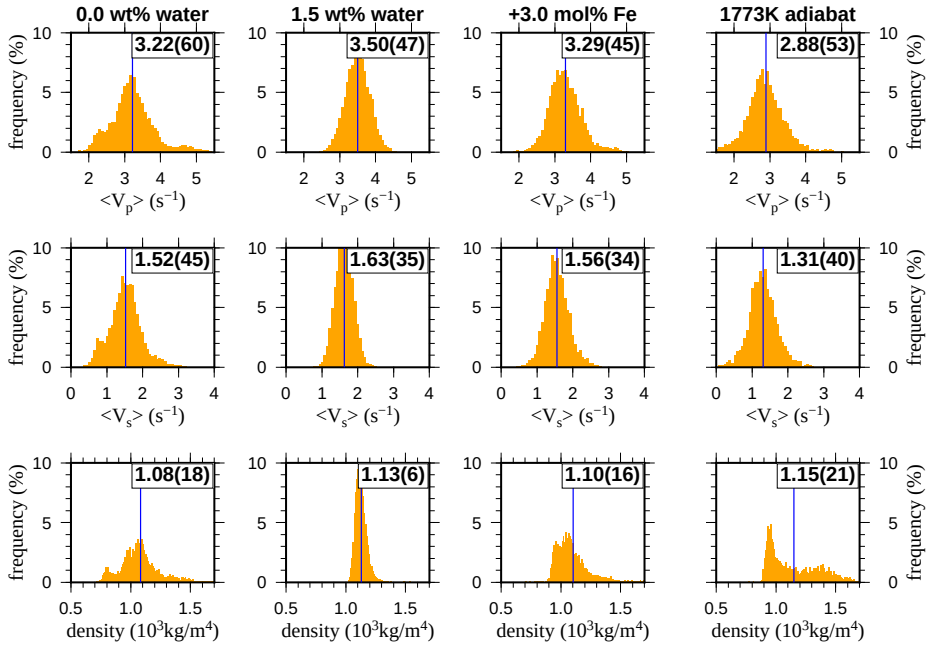

Figure 25: Average V_P, V_S and density gradients inside the transition zone for the models shown in Figure 24.

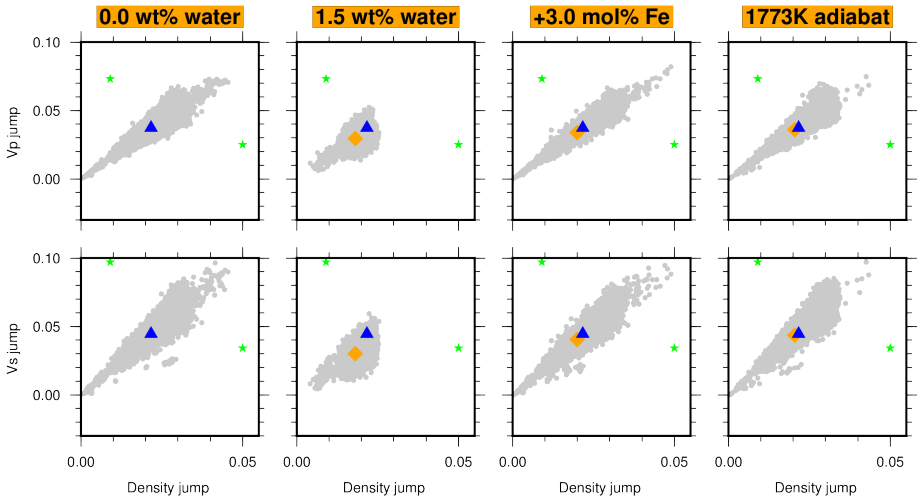

Figure 26: Impedance contrast at the '410' discontinuity. Orange diamonds indicate mean values, blue triangles correspond to the mean value of the anhydrous 1573 K adiabatic pyrolite composition. Green stars show seismic observations, see Figure 21 for reference.

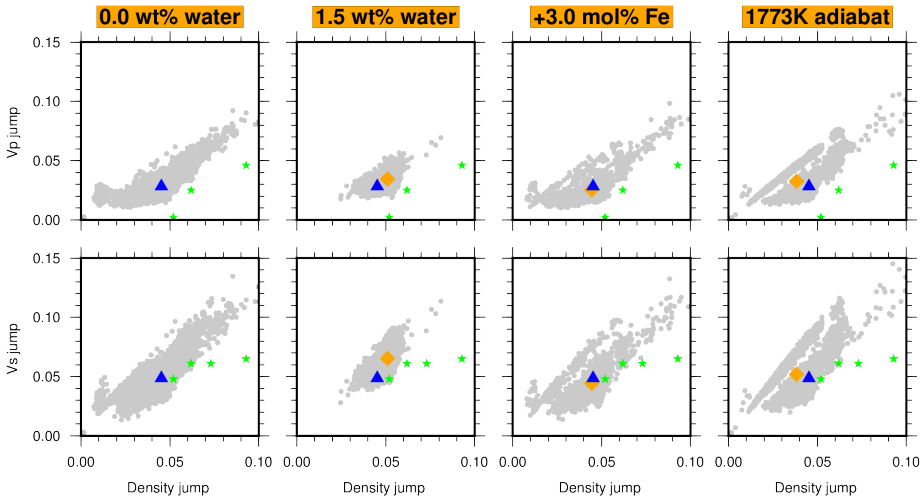

Figure 27: Impedance contrast at the '660' discontinuity, for description and references see Figures 26 and 22.

5 Discussion

5.1 Evaluation of assumptions

A model is only as good as its assumptions, so before discussing the results and possible geophysical implications, it is important to evaluate the main assumptions and their significance.

5.1.1 Constant water content per mineral

An important assumption in our modelling is having a constant water content per mineral with pressure and temperature, and predefined water partition coefficients between the NAMs. In reality, however, the storage capacities of wadsleyite and ringwoodite decrease with increasing temperature (while pressure dependence is not clear). Assuming an adiabatic P-T path, this may produce artificially high water storage capacities at the base of the depth interval in which these minerals are stable, and artificially low water storage capacities at the top of these intervals. This implies that in reality, wadsleyite has a higher water content at the top of the transition zone, compared to the overall water content that we assumed in our models. This, in turn, suggests a lower velocity at the top of the transition zone. By the same reasoning, ringwoodite has a lower water content at the base of the transition zone, resulting in a higher realistic velocities compared to the velocities found in our models. The difference in velocity between the top and bottom of the transition zone might therefore be larger than what we found in our models, which means that the average gradients might be even higher than what we derived from our models.

However, the relatively high water content of wadsleyite and relatively low water content of ringwoodite at the wadsleyite-ringwoodite phase boundary, suggest that the water partition coefficient might be smaller than the one we used in our models ($D_{wad/ring} = 2$). A smaller partition coefficient results in a smaller contrast between the velocities in wadsleyite and ringwoodite, and therefore decreases the overall velocity gradient in the transition zone. Considering the water storage capacities shown in Figure 1, wadsleyite and ringwoodite could both have a storage capacity of about 1 wt% water at the wadsleyite-ringwoodite phase boundary, resulting in a $D_{wad/ring}$ of 1.

The partition coefficient used in our models is 1:6:3 for olivine:wadsleyite:ringwoodite, and models are derived from the water content of wadsleyite. Therefore, to get an impression of the effect of equal water partitioning between wadsleyite and ringwoodite, we can combine the average velocity at the base of the transition zone of the 2.0 wt% water model (1 wt% for ringwoodite) with the average velocity at the top of the transition zone of the 1.0 wt% model. This results in an assumed overall water content of the transition zone of 1 wt% water. The resulting gradients are 3.23 s^{-1} for V_{P} and 1.35 s^{-1} for V_{S}. Compared to the gradients we found in our anhydrous ($V_{\mathrm{P}} = 3.22(60)$ s^{-1}, $V_{\mathrm{S}} = 1.52(45)$ s^{-1}), 1.0 wt% water ($V_{\mathrm{P}} = 3.33(43)$ s^{-1}, $V_{\mathrm{S}} = 1.51(36)$ s^{-1}) and 2.0 wt% water ($V_{\mathrm{P}} = 3.67(51)$ s^{-1}, $V_{\mathrm{S}} = 1.75(34)$ s^{-1}) models, this shows that the partitioning has a major influence on the average velocity gradients.

For olivine, increasing pressure increases the storage capacity so the water content at the phase transition with wadsleyite might be higher than the average value which we assumed in our modelling (from Figure 1). Therefore, the difference in water content between olivine and wadsleyite at the phase boundary might be smaller than what we anticipated from the assumed average values derived in Figure 1. This, in turn, could have major consequences on the impedance contrast at the '410' discontinuity: Since water decreases the wave speed inside the NAMs, a lower partition coefficient

increases the velocity jumps and corresponding impedance contrasts. Using the same method as described above, we find jumps in V_P, V_S and density of 0.035, 0.04 and 0.02 respectively, for a partition coefficient $D_{wad/oli}$ of 3 and a wadsleyite water content of 1 wt%. Comparing these results and those found for $D_{wad/oli} = 6$ and a water content of 1.0 wt% wadsleyite (0.034(8) for V_P, 0.038(11) for V_S and 0.020(4) for density) with the velocity and density jumps in the anhydrous model (0.037(15) (V_P), 0.046(18) (V_S) and 0.021(8) (density)), and considering the uncertainties, we see that a decrease in partition coefficient of 50 % does not significantly change the impedance contrast at the '410' discontinuity.

5.1.2 Phase boundaries

Phase boundaries in the pure-Mg system have been taken conservatively to include all data points, resulting in a wide range of possible phase boundaries. Most experiments are performed between 1300 and 1673 K, whereas for a 1573 K adiabat we expect transition zone temperatures to lie in the range 1700-1950 K. Therefore, we were required to do an extrapolation of the available data to get constraints on the phase boundaries in our area of interest. Since extrapolation is always more uncertain than interpolation, this increases the uncertainty on the position of the phase boundaries. For the Fe/Mg-mixed system, even less data was available at high pressure and temperature, especially above 1673 K. The position of the phase boundary may influence the average velocity through the transition zone, so this should be taken into account when interpreting the results we found for the whole transition zone. This is particularly important for the gradients, since these are calculated by dividing the difference at the top and bottom of the transition zone by the total thickness. A thickness difference of several tens of kilometers could therefore alter the average gradients significantly. In our models, however, the influence of the phase boundary appears to be small. For the interval between 450 and 600 km, the influence of the phase boundaries should be significantly less.

Also important to note here is the effect of the pressure scale on the uncertainties on the experimental data used to derive the phase boundaries. Experiments on the post-spinel phase boundary by Litasov et al. (2005) and Ghosh et al. (2013), who used a different Au pressure scale, indicate that the choice of pressure scale can influence the result by almost 1 GPa, which is about 25 km in depth. Compared to the uncertainty on the pressure of the ringwoodite-perovskite phase boundary in our models, which is up to ∼2 GPa (Figure 5) or ∼50 km, this could have a major influence on the position of the phase boundary.

5.1.2.1 Helmholtz free energy (F_0) values

The F_0 of the NAMs were determined iteratively from data on the phase boundaries between olivine, its high-pressure polymorphs and perovksite, and are therefore correlated with each other. We did not, however, correlate the new F_0 values with those of the other potential stable minerals in the transition zone (e.g. garnet) because no data was available to do so. This could result in some minerals being stable at pressure and temperature conditions where they should not be stable. In case of the garnet to perovskite phase transition (see below), a bad correlation between the F_0 values could result in a shallower or deeper phase transition, which in turn could effect the position of the '660' discontinuity.

5.1.2.2 The garnet-perovskite phase transition

Though the ringwoodite-perovskite phase transition is generally thought to be the main reason behind the sharp velocity increase at the '660' discontinuity, another phase transition to take into consideration is the garnet to perovskite phase transition. Irifune et al. (1996), who looked at phase transitions in the system $MgSiO_3$-$Mg_3Al_2Si_3O_{12}$, found that for compositions with up to 15 mol% Al, a sequence of phase transformations occurs between 22 and 24 GPa (at 1773 K) that involve garnet. This pressure interval corresponds to a depth interval between 625 and 675 km, indicating that the '660' discontinuity found in seismic observations, might be (partly) the result of phase transitions of garnet. Since we correlate the stability of perovskite with ringwoodite (and not with garnet) in our models, this might effect the position of the phase boundary between garnet and perovskite, which could ultimately effect the computed seismic profile. The garnet-perovskite phase transition could also explain why we found a bimodel distribution at the '660' discontinuity in some of our models.

5.1.3 Fe endmember elastic properties

The elastic properties for the Fe endmember of each mineral are poorly constrained and therefore a major concern in our computations. The effect of the large uncertainties is clearly shown in the FeO-SiO2-MgO system, where the range of velocity and density profiles covers a large area (Figure 7). In the pyrolite composition, on the other hand (Figure 12), the range is much smaller, indicating that the mineral properties of the Fe-endmember are of less importance there. *Perple_x* uses the elastic properties at the endmembers of a mineral to calculate the overall elastic properties of that mineral in solid solution. Since pyrolite consists of both MgO and FeO, the NAMs are in solid solution and the elastic properties per NAM are a function of the elastic properties of the Fe and Mg endmember. The elastic properties of the Fe-endmembers have been obtained with broad assumption and extrapolation from limited data points and we should be aware of this (unavoidable) limitation in our modelling.

5.1.4 Parameter uncertainties

Except for those of hydrous olivine, hydrous wadsleyite and hydrous ringwoodite, all mineral parameters have been taken from the compiled dataset of Stixrude and Lithgow-Bertelloni (2011). Since these have been obtained simultaneously by a global inversion, a correlation between these parameters almost certainly exists but has not been published. Therefore, we assumed all parameters to be independent of one another, and varied them at random within the published uncertainties of Stixrude and Lithgow-Bertelloni (2011). However, this assumption most likely leads to a gross overestimation of the uncertainty in the mineral seismic properties, since it does not take into account the correlation between the different elastic parameters. This is the case even when we restricted the uncertainty analysis to the three NAMs, olivine, wadsleyite and ringwoodite. This most likely explains, for example, why the uncertainty on the depths of the '410' and '660' discontinuities is always greater for the anhydrous than the hydrous models (e.g. Figure 12): in the former, F_0 and θ_0 are uncorrelated whereas in the latter they are implicitly correlated during our procedure to fit the published phase equilibria. Thus, if the correlation matrix for the elastic parameters of Stixrude and Lithgow-Bertelloni (2011) would become available, we anticipate that the uncertainty in our anhydrous models would be significantly reduced.

In addition to the correlations between mineral parameters imposed by the inversion procedure of

Stixrude and Lithgow-Bertelloni (2011), experimentally-derived mineral parameters are also often correlated. This is particularly the case for K_0 and dK/dP, and G_0 and dG/dP (J. Jackson, personal communication 2014). However these correlation coefficients are also typically not published. For all our hydrous models, we determined K_0, G_0, dK/dP and dG/dP independently for each run by randomly picking a value within the ranges shown in Figures 3 and 4. Knowing the correlation between K_0, G_0 and dK/dP, dG/dP reduces the uncertainties of the pressure derivatives once the bulk and shear moduli have been (randomly) picked, which ultimately results in an overall smaller uncertainty of the models. Therefore, we likely have an overestimation of the uncertainties in our models.

It has recently come to light that the high values of the pressure derivatives of the bulk and shear moduli (dK/dP and dG/dP) of hydrous ringwoodite, as measured by XRD experiments, may not be reliable (J. Jackson, personal communication 2014). This implies that the bulk and shear moduli of hydrous ringwoodite may increase more slowly with increasing pressure than what we modelled, which ultimately means that the wavespeeds in ringwoodite are less than what we predicted in our models. This, in turn, implies that some models might have too high pressure derivatives of K and G, and that the average values of the velocity gradients in the transition zone might be overestimated.

5.1.5 Solid solution model including $[OH]^-$

A limitation of *Perple_x* is that it requires a constant bulk composition, and that water (in the form of OH^-) is not a free input parameter. We therefore assumed for each run an anhydrous bulk composition as input to *Perple_x*, and altered only the elastic properties of the NAMs to account for the effects of water. A more precise method would be to include OH^- in the bulk composition and come up with a $[OH]^- - Mg - Fe$ solid-solution model for olivine, wadsleyite and ringwoodite. We did not do this for two main reasons: 1) limited data is available for the solid-solution models of hydrous olivine, wadsleyite and ringwoodite, and 2) OH^- is not (yet) included as a free parameter in *Perple_x*. Implementing a $[OH]^- - Mg - Fe$ solid-solution model into *Perple_x* requires a significant amount of programming and is beyond the scope of this project.

5.2 Uncertainties and limitations of seismic observations

To fully understand the relationship between mineral physics and synthetic models on one side, and seismic observations on the other, it is important to also understand the uncertainties and limitations of seismic observations. In seismology, the depths of the '410' and '660' discontinuities are relatively easy to constrain, though the effect of topography and the process of data averaging might give rise to some complications. The uncertainty on the position of the discontinuities (or vertical resolution) varies between studies depending on the data type and scale of the study, but can be as little as 8 km (Lessing et al., 2014), which is about 0.3 GPa. Assuming that the discontinuities are caused by the phase transitions between olivine and its high-pressure polymorphs, this means that the phase boundaries between hydrous olivine, wadsleyite, ringwoodite and perovskite should be constrained within an uncertainty of 0.3 GPa. From our synthetic models we find that the average velocity gradients are the best feature to distinguish between changes in composition/temperature and water presence in the transition zone. These gradients, however, are very difficult to obtain from seismic observations, though it might be possible to obtain them from surface waves. Other seismic observations, include average velocities of the transition zone (easy to constrain once the

discontinuity depths are fixed) and the density, which is extremely hard to constrain. According to our synthetic models, however, these observations are less relevant when trying to identify the presence of water in the mantle transition zone.

5.3 Discontinuity depths and transition zone thickness

'660' discontinuity - The mean depth of the '660' discontinuity in all our hydrous pyrolite models is 630 km, which is much shallower than the depth found in seismic reference models (e.g. PREM (670 km) and AK135 (660 km)). Houser et al. (2008), using SS precursors to produce a global map of the '660' discontinuity, report a variation of more than 17 km relative to a reference depth of 660 km. The shallowest region they found is underneath eastern Africa, where the '660' discontinuity is at a depth of about ∼643 km. A regional SS and PP undersides study of India and Western China by Lessing et al. (2014), found depths between 660 and 700 km but also large areas where the '660' was not detected. Day and Deuss (2014) also found variations up to 34 km, relative to a reference depth of 660 km, using PP and P'P' precursors. These depths, however, are still 10 km deeper than the mean value we found in our study.

'410' discontinuity - The mean depth of the '410' discontinuity in our hydrous pyrolite models (408 km) is much closer to those found in seismic models (e.g. PREM (400 km) and AK135 (410 km)). A global study of '410' PP and SS precursors by Chambers et al. (2005a) reports variations of up to 30 km relative to the reference depth of 410 km, which is a much larger range than what we obtained in this study. Lessing et al. (2014) found an elevation of the '410' in the Tian Shan region and Eastern Himalayas, up to 370-390 km. Below Tibet and Western-China they found a depression of 410-440 km.

Transition zone thickness - Due to our elevated '660' discontinuity, the average thickness of the mantle transition zone found in this study is relatively small (220 km). Other studies on the thickness of the transition zone report thicknesses ranging from 210-270 km (Deuss, 2009; Houser et al., 2008; Lawrence and Shearer, 2008), but locations where the transition zone is thin vary between these models.

Considering the uncertainty on the position of the phase boundary in our models (∼2 GPa or 50 km, Figure 5), together with the uncertainty of the experimental data due to the pressure scale (1 GPa or 25 km) and the vertical resolution of seismic observations (e.g. 8 km Lessing et al., 2014) we cannot draw any conclusion about whether the depth of the discontinuities and the thickness of the transition zone can be used to search for water in the transition zone.

5.4 Implications

It is clear from our models that water can have a significant effect on the seismic structure of the transition zone. An increase in water content causes a decrease in average density and velocities and an increase in average velocity and density gradients. Furthermore, water influences the impedance contrast at the '410' and '660' discontinuities, depending specifically on the water partitioning between the minerals of the corresponding phase transitions. Other thermochemical effects (e.g. Fe-rich pyrolite, alternative thermal structure) also change the seismic profile, but none of these result in the same combination of velocity and density decrease, velocity gradient increase and change in velocity jumps at the discontinuities. This suggests that it may be possible to derive the quantity and distribution of water in the transition zone from seismic observations.

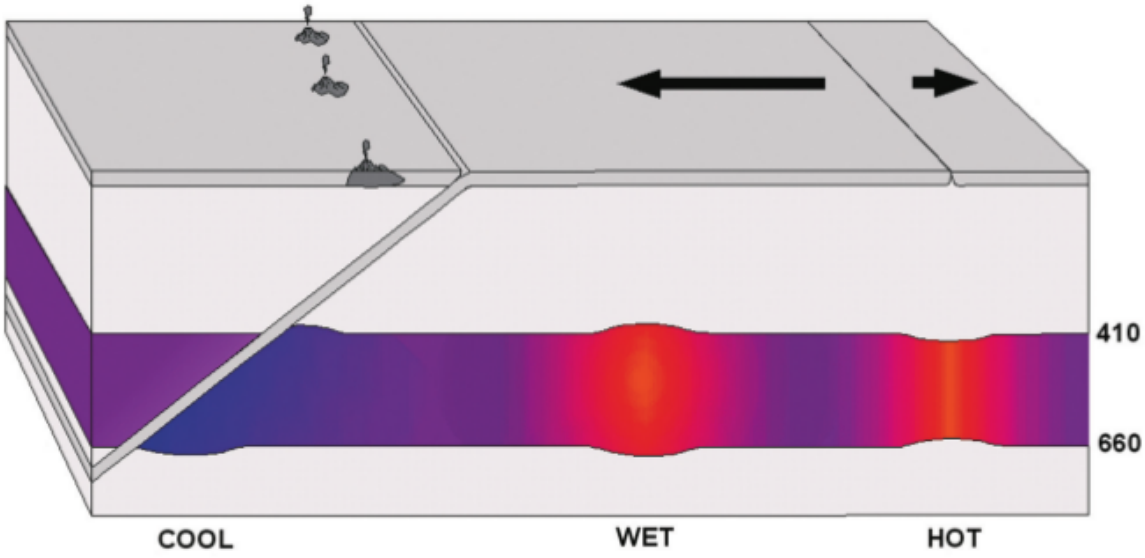

Figure 28: A schematic drawing of the conventional view of the contrasting effects of hot upwelling (right), hydrous (center), and a cold, subducting (left) regions of the Transition Zone, where blue indicates seismically fast and red indicates slow regions. A shallow 410 and deep 660 with intervening low V_S and elevated V_P/V_S ratios would indicate hydrous conditions in the Transition Zone. Our results indicate that this "conventional" model may need re-assessment. From: Smyth and Jacobsen (2006)

However, taking into account the uncertainties of our input parameters and the evaluation of our assumptions, together with the limitations and uncertainties of seismic observations, we do not venture to draw such a conclusion. As changing the partition coefficients and varying the water content per mineral as a function of pressure and temperature can have a significant impact on the seismic structure, a better constraint on these parameters is necessary before a firm statement can be made about the relationship between water content of the transition zone and seismic observations.

Of particular importance is the trade-off between temperature and water effects. Our models indicate that an increased water content or temperature both result in lower average velocities of the mantle transition zone, which is in agreement with most previous studies (e.g. Smyth and Jacobsen, 2006). However, using our compiled dataset of the phase transitions between olivine and its high pressure polymorphs under hydrous conditions, we do not see an elevation of the '410' discontinuity, nor a depression of the '660' discontinuity (our '660' is even elevated), as is also suggested by the same studies. This poses the question whether it is correct to assume that a thick and slow transition zone always indicates the presence of water (see Figure 28, from Smyth and Jacobsen (2006)). If this is not necessarily the case, then it is possible that previous seismic studies regarding the water content in the transition zone (e.g. Meier et al., 2009; Houser, 2014), might have overinterpreted their results.

5.5 Future work

It is clear from our study that more work needs to be done to improve synthetic seismic modelling of the hydrous transition zone and to better understand the relationship between mineral physics

data and seismic observations. Here we summarize our most important recommendations for future work:

1. Data on the phase transition between hydrous olivine, wadsleyite, ringwoodite and perovskite (specifically Fe/Mg solid solutions, e.g. Fo90) at high temperatures (1800-2000 K) is needed to get a better constraint on the position of the phase boundaries. These phase boundaries should be determined within an uncertainty of about 0.3 GPa, which corresponds to 8 km (vertical resolution of seismic observations, e.g. Lessing et al., 2014). In addition, more data is needed on the storage capacities of these minerals as a function of pressure, temperature (specifically above 1800 K) and composition (Fe content).

2. We assumed that temperature derivatives of the bulk and shear moduli per mineral did not change with increasing water content. To account for the change in temperature dependence of the elastic properties as a function of water content, data is needed for q_0, η_0 and γ per mineral at hydrous conditions.

3. In thermodynamic modelling, changing the water content per phase as a function of pressure and temperature would greatly improve the synthetic seismic models. This would also mean that the partition coefficients between the minerals do not have to be determined prior to running the model. In *Perple_x*, this would mean including OH^- as a free parameter in determination of the phase equilibria and allowing for a free fluid phase (and other hydrous phases/minerals).

4. Another modelling improvement would be if elastic properties of the solid solutions could be used directly as input, instead of the elastic properties at the endmembers of the minerals. This would greatly reduce the uncertainty of the model since these elastic properties can be measured directly per mineral. Alternatively, experimental data on the elastic properties at the pure Fe endmembers (Fe_2SiO_4) would greatly reduce the uncertainties at these endmembers.

5. A correlation exists between the bulk and shear moduli and their corresponding pressure derivatives, but this data has not been published. Making this data available would reduce the uncertainties of these parameters and consequently result in smaller uncertainties in the final models.

Of these recommendations, the most important one is to obtain new measurements for a better constraint on the phase boundaries, because the phase boundaries have a major influence on the synthetic models and because the discontinuity depths are relatively easy to constrain from seismic observations. This requires experiments at high pressure and temperature, which is very difficult because it is not possible to measure the composition at high pressure and temperature. Instead, samples must be quenched to low pressure and temperature to check if they are hydrous. The most straightforward and easiest to obtain of these recommendations is probably the correlation between K_0, G_0 and K', G', which would significantly reduce the uncertainty space of the models and potentially allow tighter constraints on the velocities and velocity gradients.

6 Acknowledgments

I would like to express my great appreciation to Dr Laura Cobden, who spend a generous amount of time supervising the project with constructive criticism, enthusiasm and encouragement. Furthermore, I would like to thank Prof. Dr Jeannot Trampert for co-supervising the project and his

feedback.

References

Anderson, D. L. (2007). *New theory of the Earth*. Cambridge University Press.

Anderson, O. L. (1963). A simplified method for calculating the debye temperature from elastic constants. *Journal of Physics and Chemistry of Solids*, 24(7):909–917.

Anderson, O. L. (1995). Equations of state of solids for geophysics and ceramic science.

Aubaud, C., Hirschmann, M. M., Withers, A. C., and Hervig, R. L. (2008). Hydrogen partitioning between melt, clinopyroxene, and garnet at 3 gpa in a hydrous morb with 6 wt. *Contributions to Mineralogy and Petrology*, 156(5):607–625.

Barron, T., Berg, W., and Morrison, J. (1957). The thermal properties of alkali halide crystals. ii. analysis of experimental results. *Proceedings of the Royal Society of London.Series A.Mathematical and Physical Sciences*, 242(1231):478–492.

Bercovici, D. and Karato, S. I. (2003). Whole-mantle convection and the transition-zone water filter. *Nature*, 425(6953):39–44.

Blackman, M. (1955). The specific heat of solids. *Handbuch der Physik*, 7:325–382.

Bolfan-Casanova, N., Keppler, H., and Rubie, D. C. (2000). Water partitioning between nominally anhydrous minerals in the mgo-sio2-h2o system up to 24 gpa: implications for the distribution of water in the earth's mantle. *Earth and Planetary Science Letters*, 182(3-4):209–221.

Castle, J. C. and Creager, K. C. (2000). Local sharpness and shear wave speed jump across the 660-km discontinuity. *Journal of Geophysical Research: Solid Earth (1978–2012)*, 105(B3):6191–6200.

Chambers, K., Deuss, A., and Woodhouse, J. (2005a). Reflectivity of the 410-km discontinuity from pp and ss precursors. *Journal of Geophysical Research: Solid Earth (1978-2012)*, 110(B2).

Chambers, K., Woodhouse, J., and Deuss, A. (2005b). Topography of the 410-km discontinuity from pp and ss precursors. *Earth and Planetary Science Letters*, 235(3):610–622.

Chen, J., Inoue, T., Weidner, D. J., Wu, Y., and Vaughan, M. T. (1998). Strength and water weakening of mantle minerals, olivine, wadsleyite and ringwoodite. *Geophysical Research Letters*, 25(4):575–578.

Chen, J. H., Inoue, T., Yurimoto, H., and Weidner, D. J. (2002). Effect of water on olivine-wadsleyite phase boundary in the (mg, fe)(2)sio4 system. *Geophysical Research Letters*, 29(18):1875.

Cobden, L., Goes, S., Cammarano, F., and Connolly, J. A. (2008). Thermochemical interpretation of one-dimensional seismic reference models for the upper mantle: evidence for bias due to heterogeneity. *Geophysical Journal International*, 175(2):627–648.

Connolly, J. (1990). Multivariable phase diagrams; an algorithm based on generalized thermodynamics. *American Journal of Science*, 290(6):666–718.

Connolly, J. (2005). Computation of phase equilibria by linear programming: a tool for geodynamic modeling and its application to subduction zone decarbonation. *Earth and Planetary Science Letters*, 236(1):524–541.

Daniel, I., Perez, E. C., Martinez, I., Chervin, J., and Dumas, P. (2003). High-pressure behavior of protonated wadsleyite: an ir spectroscopic study. In *EGS-AGU-EUG Joint Assembly*, volume 1, page 5685.

Day, E. A. and Deuss, A. (2014). Reconciling pp and p'p' precursor observations of a complex 660 km seismic discontinuity. *Geophysical Journal International*.

Demouchy, S., Deloule, E., Frost, D. J., and Keppler, H. (2005). Pressure and temperature-dependence of water solubility in fe-free wadsleyite. *American Mineralogist*, 90(7):1084–1091.

Demouchy, S. and Mackwell, S. (2006). Mechanisms of hydrogen incorporation and diffusion in iron-bearing olivine. *Physics and Chemistry of Minerals*, 33(5):347–355.

Deon, F., Koch-Mueller, M., Rhede, D., and Wirth, R. (2011). Water and iron effect on the p-t-x coordinates of the 410-km discontinuity in the earth upper mantle. *Contributions to Mineralogy and Petrology*, 161(4):653–666.

Deuss, A. (2009). Global observations of mantle discontinuities using ss and pp precursors. *Surveys in Geophysics*, 30(4-5):301–326.

Dixon, J. E., Leist, L., Langmuir, C., and Schilling, J.-G. (2002). Recycled dehydrated lithosphere observed in plume-influenced mid-ocean-ridge basalt. *Nature*, 420(6914):385–389.

Drake, M. J. (2005). Origin of water in the terrestrial planets. *Meteoritics & Planetary Science*, 40(4):519–527.

Dziewonski, A. M. and Anderson, D. L. (1981). Preliminary reference earth model. *Physics of the earth and planetary interiors*, 25(4):297–356.

Estabrook, C. H. and Kind, R. (1996). The nature of the 660-kilometer upper-mantle seismic discontinuity from precursors to the pp phase. *Science*, 274(5290):1179–1182.

Ferot, A. and Bolfan-Casanova, N. (2012). Water storage capacity in olivine and pyroxene to 14 gpa: Implications for the water content of the earth's upper mantle and nature of seismic discontinuities. *Earth and Planetary Science Letters*, 349:218–230.

Ganskow, G., Ballaran, T. B., and Langenhorst, F. (2010). Effect of iron on the compressibility of hydrous ringwoodite. *American Mineralogist*, 95(5-6):747–753.

Ghosh, S., Ohtani, E., Litasov, K. D., Suzuki, A., Dobson, D., and Funakoshi, K. (2013). Effect of water in depleted mantle on post-spinel transition and implication for 660 km seismic discontinuity. *Earth and Planetary Science Letters*, 371:103–111.

Higo, Y., Inoue, T., Li, B., Irifune, T., and Liebermann, R. C. (2006). The effect of iron on the elastic properties of ringwoodite at high pressure. *Physics of the Earth and Planetary Interiors*, 159(3-4):276–285.

Hill, T. L. (2012). *An introduction to statistical thermodynamics*. Courier Dover Publications.

Hirschmann, M. M. (2006). Water, melting, and the deep earth h2o cycle. *Annu.Rev.Earth Planet.Sci.*, 34:629–653.

Holl, C. M., Smyth, J. R., Jacobsen, S. D., and Frost, D. J. (2008). Effects of hydration on the structure and compressibility of wadsleyite, beta-(mg2sio4). *American Mineralogist*, 93(4):598–607.

Houser, C. (2014). The absence of water in the mantle transition zone according to seismic data (abstract). *SEDI conference, Japan 2014*.

Houser, C., Masters, G., Flanagan, M., and Shearer, P. (2008). Determination and analysis of long-wavelength transition zone structure using ss precursors. *Geophysical Journal International*, 174(1):178–194.

Inoue, T., Tanimoto, Y., Irifune, T., Suzuki, T., Fukui, H., and Ohtaka, O. (2004). Thermal expansion of wadsleyite, ringwoodite, hydrous wadsleyite and hydrous ringwoodite. *Physics of the Earth and Planetary Interiors*, 143:279–290.

Inoue, T., Ueda, T., Tanimoto, Y., Yamada, A., and Irifune, T. (2010a). The effect of water on the high-pressure phase boundaries in the system mg(2)sio(4)-fe(2)sio(4). *International Conference on High Pressure Science and Technology, Joint Airapt-22 and Hpcj-50*, 215:012101.

Inoue, T., Wada, T., Sasaki, R., and Yurimoto, H. (2010b). Water partitioning in the earth's mantle. *Physics of the Earth and Planetary Interiors*, 183(1-2):245–251.

Inoue, T., Weidner, D. J., Northrup, P. A., and Parise, J. B. (1998). Elastic properties of hydrous ringwoodite (gamma-phase) in mg2sio4. *Earth and Planetary Science Letters*, 160(1-2):107–113.

Inoue, T., Yurimoto, H., and Kudoh, Y. (1995). Hydrous modified spinel, mg1.75sih0.5o4: a new water reservoir in the mantle transition region. *Geophysical Research Letters*, 22(2):117–120.

Irifune, T., Koizumi, T., and ichi Ando, J. (1996). An experimental study of the garnet-perovskite transformation in the system mgsio¡ sub¿ 3¡/sub¿ mg¡ sub¿ 3¡/sub¿ al¡ sub¿ 2¡/sub¿ si¡ sub¿ 3¡/sub¿ o¡ sub¿ 12¡/sub¿. *Physics of the Earth and Planetary Interiors*, 96(2):147–157.

Jacobsen, S. D., Demouchy, S., Frost, D. J., Ballaran, T. B., and Kung, J. (2005). A systematic study of oh in hydrous wadsleyite from polarized ftir spectroscopy and single-crystal x-ray diffraction: Oxygen sites for hydrogen storage in earth's interior. *American Mineralogist*, 90(1):61–70.

Jacobsen, S. D., Jiang, F., Mao, Z., Duffy, T. S., Smyth, J. R., Holl, C. M., and Frost, D. J. (2008). Effects of hydration on the elastic properties of olivine. *Geophysical Research Letters*, 35(14):L14303.

Jacobsen, S. D. and Smyth, J. R. (2006). Effect of water on the sound velocities of ringwoodite in the transition zone. *Geophysical Monograph Series*, 168:131–145.

Jacobsen, S. D., Smyth, J. R., Spetzler, H., Holl, C. M., and Frost, D. J. (2004). Sound velocities and elastic constants of iron-bearing hydrous ringwoodite. *Physics of the Earth and Planetary Interiors*, 143-144(0):47–56.

Kawamoto, T., Hervig, R. L., and Holloway, J. R. (1996). Experimental evidence for a hydrous transition zone in the early earth's mantle. *Earth and Planetary Science Letters*, 142(3):587–592.

Kennett, B., Engdahl, E., and Buland, R. (1995). Constraints on seismic velocities in the earth from traveltimes. *Geophysical Journal International*, 122(1):108–124.

Kohlstedt, D. L., Keppler, H., and Rubie, D. C. (1996). Solubility of water in the alpha, beta and gamma phases of (mg,fe)(2)sio4. *Contributions to Mineralogy and Petrology*, 123(4):345–357.

Kudoh, Y., Kuribayashi, T., Mizobata, H., and Ohtani, E. (2000). Structure and cation disorder of hydrous ringwoodite, gamma-mg1.89si0.98h0.30o4. *Physics and Chemistry of Minerals*, 27(7):474–479.

Lawrence, J. F. and Shearer, P. M. (2008). Imaging mantle transition zone thickness with sds-ss finite-frequency sensitivity kernels. *Geophysical Journal International*, 174(1):143–158.

Lessing, S., Thomas, C., Rost, S., Cobden, L., and Dobson, D. P. (2014). Mantle transition zone structure beneath india and western china from migration of pp and ss precursors. *Geophysical Journal International*, 197(1):396–413.

Litasov, K. and Ohtani, E. (2003). Stability of various hydrous phases in cmas pyrolite-h2o system up to 25 gpa. *Physics and Chemistry of Minerals*, 30(3):147–156.

Litasov, K. and Ohtani, E. (2008). Systematic study of hydrogen incorporation into fe-bearing wadsleyite and water storage capacity of the transition zone. *Water Dynamics*, 987:113–118.

Litasov, K. D., Ohtani, E., Kagi, H., Jacobsen, S. D., and Ghosh, S. (2007). Temperature dependence and mechanism of hydrogen incorporation in olivine at 12.5-14.0 gpa. *Geophysical Research Letters*, 34(16):L16314.

Litasov, K. D., Ohtani, E., Sano, A., Suzuki, A., and Funakoshi, K. (2005). Wet subduction versus cold subduction. *Geophysical Research Letters*, 32(13):L13312.

Litasov, K. D., Shatskiy, A., Ohtani, E., and Katsura, T. (2011). Systematic study of hydrogen incorporation into fe-free wadsleyite. *Physics and Chemistry of Minerals*, 38(1):75–84.

Manghnani, M. H., Amulele, G., Smyth, J. R., Holl, C. M., Chen, G., Prakapenka, V., and Frost, D. J. (2005). Equation of state of hydrous fo(90) ringwoodite to 45 gpa by synchrotron powder diffraction. *Mineralogical Magazine*, 69(3):317–323.

Mao, Z., Jacobsen, S. D., Frost, D. J., McCammon, C. A., Hauri, E. H., and Duffy, T. S. (2011). Effect of hydration on the single-crystal elasticity of fe-bearing wadsleyite to 12 gpa. *American Mineralogist*, 96(10):1606–1612.

Mao, Z., Jacobsen, S. D., Jiang, F., Smyth, J. R., Holl, C. M., and Duffy, T. S. (2008a). Elasticity of hydrous wadsleyite to 12 gpa: Implications for earth's transition zone. *Geophysical Research Letters*, 35(21):L21305.

Mao, Z., Jacobsen, S. D., Jiang, F., Smyth, J. R., Holl, C. M., Frost, D. J., and Duffy, T. S. (2010). Velocity crossover between hydrous and anhydrous forsterite at high pressures. *Earth and Planetary Science Letters*, 293(3-4):250–258.

Mao, Z., Jacobsen, S. D., Jiang, F. M., Smyth, J. R., Holl, C. M., Frost, D. J., and Duffy, T. S. (2008b). Single-crystal elasticity of wadsleyites, beta-mg2sio4, containing 0.37-1.66 wt. *Earth and Planetary Science Letters*, 268(3-4):540–549.

Mao, Z., Lin, J.-F., Jacobsen, S. D., Duffy, T. S., Chang, Y.-Y., Smyth, J. R., Frost, D. J., Hauri, E. H., and Prakapenka, V. B. (2012). Sound velocities of hydrous ringwoodite to 16 gpa and 673 k. *Earth and Planetary Science Letters*, 331:112–119.

Meier, U., Trampert, J., and Curtis, A. (2009). Global variations of temperature and water content in the mantle transition zone from higher mode surface waves. *Earth and Planetary Science Letters*, 282(1):91–101.

Mosenfelder, J. L., Deligne, N. I., Asimow, P. D., and Rossman, G. R. (2006). Hydrogen incorporation in olivine from 2-12 gpa. *American Mineralogist*, 91(2-3):285–294.

Ohtani, E., Mizobata, H., and Yurimoto, H. (2000). Stability of dense hydrous magnesium silicate phases in the systems mg2sio4-h2o and mgsio3-h2o at pressures up to 27 gpa. *Physics and Chemistry of Minerals*, 27(8):533–544.

Panero, W. R. (2010). First principles determination of the structure and elasticity of hydrous ringwoodite. *Journal of Geophysical Research-Solid Earth*, 115:B03203.

Pearson, D., Brenker, F., Nestola, F., McNeill, J., Nasdala, L., Hutchison, M., Matveev, S., Mather, K., Silversmit, G., and Schmitz, S. (2014). Hydrous mantle transition zone indicated by ringwoodite included within diamond. *Nature*, 507(7491):221–224.

Poirier, J.-P. (2000). *Introduction to the Physics of the Earth's Interior*. Cambridge University Press.

Regenauer-Lieb, K., Yuen, D. A., and Branlund, J. (2001). The initiation of subduction: criticality by addition of water? *Science (New York, N.Y.)*, 294(5542):578–580. LR: 20070319; JID: 0404511; ppublish.

Revenaugh, J. and Jordan, T. H. (1991). Mantle layering from scs reverberations: 1. waveform inversion of zeroth-order reverberations. *Journal of Geophysical Research: Solid Earth (1978–2012)*, 96(B12):19749–19762.

Richard, G., Monnereau, M., and Rabinowicz, M. (2007). Slab dehydration and fluid migration at the base of the upper mantle: implications for deep earthquake mechanisms. *Geophysical Journal International*, 168(3):1291–1304.

Rost, S. and Weber, M. (2002). The upper mantle transition zone discontinuities in the pacific as determined by short-period array data. *Earth and Planetary Science Letters*, 204(3):347–361.

Rupke, L., Morgan, J. P., and Dixon, J. E. (2006). Implications of subduction rehydration for earth's deep water cycle. *Earth's Deep Water Cycle*, pages 263–276.

Shearer, P. M. (1991). Constraints on upper mantle discontinuities from observations of long-period reflected and converted phases. *Journal of Geophysical Research: Solid Earth (1978-2012)*, 96(B11):18147–18182.

Shearer, P. M. (1996). Transition zone velocity gradients and the 520-km discontinuity. *Journal of Geophysical Research: Solid Earth (1978–2012)*, 101(B2):3053–3066.

Shearer, P. M. and Flanagan, M. P. (1999). Seismic velocity and density jumps across the 410-and 660-kilometer discontinuities. *Science*, 285(5433):1545–1548.

Smyth, J., Frost, D., Nestola, F., Holl, C., and Bromiley, G. (2006). Olivine hydration in the deep upper mantle: effects of temperature and silica activity. *Geophysical Research Letters*, 33(15).

Smyth, J. R. (1987). Beta-mg2sio4 - a potential host for water in the mantle. *American Mineralogist*, 72(11-12):1051–1055.

Smyth, J. R. and Frost, D. J. (2002). The effect of water on the 410-km discontinuity: An experimental study. *Geophysical Research Letters*, 29(10):1485.

Smyth, J. R., Frost, D. J., and Nestola, F. (2005). Hydration of olivine and the earth's deep water cycle. *Geochim. Cosmochim. Acta*, 69:A746.

Smyth, J. R., Holl, C. M., Frost, D. J., Jacobsen, S. D., Langenhorst, F., and McCammon, C. A. (2003). Structural systematics of hydrous ringwoodite and water in earth's interior. *American Mineralogist*, 88(10):1402–1407.

Smyth, J. R. and Jacobsen, S. D. (2006). *Nominally anhydrous minerals and Earth's deep water cycle*, volume 168. American Geophysical Union.

Stixrude, L. and Lithgow-Bertelloni, C. (2005). Thermodynamics of mantle minerals - i. physical properties. *Geophysical Journal International*, 162(2):610–632.

Stixrude, L. and Lithgow-Bertelloni, C. (2011). Thermodynamics of mantle minerals - ii. phase equilibria. *Geophysical Journal International*, 184(3):1180–1213.

Sun, S.-S. (1982). Chemical composition and origin of the earth's primitive mantle. *Geochimica et Cosmochimica Acta*, 46(2):179–192.

Tian, L., Zhao, J., Liu, W., Liu, L., Liu, H., and Du, J. (2012). Effect of iron on high pressure elasticity of hydrous wadsleyite and ringwoodite by first-principles simulation. *High Pressure Research*, 32(3):385–395.

Wang, J., Sinogeikin, S. V., Inoue, T., and Bass, J. D. (2006). Elastic properties of hydrous ringwoodite at high-pressure conditions. *Geophysical Research Letters*, 33(14):L14308.

Wang, J. Y., Sinogeikin, S. V., Inoue, T., and Bass, J. D. (2003). Elastic properties of hydrous ringwoodite. *American Mineralogist*, 88(10):1608–1611.

Xu, F., Vidale, J. E., and Earle, P. S. (2003). Survey of precursors to p'p': Fine structure of mantle discontinuities. *Journal of Geophysical Research: Solid Earth (1978-2012)*, 108(B1):ETG 7–1–ETG 7–10.

Yang, X., Keppler, H., Dubrovinsky, L., and Kurnosov, A. (2014). In-situ infrared spectra of hydroxyl in wadsleyite and ringwoodite at high pressure and high temperature. *American Mineralogist*, 99(4):724–729.

Ye, Y., Brown, D. A., Smyth, J. R., Panero, W. R., Jacobsen, S. D., Chang, Y.-Y., Townsend, J. P., Thomas, S.-M., Hauri, E. H., Dera, P., and Frost, D. J. (2012). Compressibility and thermal expansion of hydrous ringwoodite with 2.5(3) wt *American Mineralogist*, 97(4):573–582.

Ye, Y., Schwering, R. A., and Smyth, J. R. (2009). Effects of hydration on thermal expansion of forsterite, wadsleyite, and ringwoodite at ambient pressure. *American Mineralogist*, 94(7):899–904.

Ye, Y., Smyth, J. R., Hushur, A., Manghnani, M. H., Lonappan, D., Dera, P., and Frost, D. J. (2010). Crystal structure of hydrous wadsleyite with 2.8% h2o and compressibility to 60 gpa. *American Mineralogist*, 95(11-12):1765–1772.

Yusa, H. and Inoue, T. (1997). Compressibility of hydrous wadsleyite (beta-phase) in mg2sio4 by high pressure x-ray diffraction. *Geophysical Research Letters*, 24(14):1831–1834.

Yusa, H., Inoue, T., and Ohishi, Y. (2000). Isothermal compressibility of hydrous ringwoodite and its relation to the mantle discontinuities. *Geophysical Research Letters*, 27(3):413–416.

Zhao, Y.-H., Ginsberg, S., and Kohlstedt, D. (2004). Solubility of hydrogen in olivine: dependence on temperature and iron content. *Contributions to Mineralogy and Petrology*, 147(2):155–161.

Appendices

A Elastic properties of olivine, wadsleyite and ringwoodite

Table 2: **Olivine**

Mg/(Mg+Fe)	$wt\%$ **water**	V_0	K_{T0}	G_0	dK/dP	dG/dP	**reference**
100	0.9(1)				4.50(5)[a]	1.75(5)	Mao et al. (2010)
100	0.8		125.7(2)[a]	79.8(1)			Jacobsen et al. (2008)
100	0.89	43.74[b]					Smyth et al. (2005)
100	0.85	43.72[b]					Smyth et al. (2005)
100	0.56	43.7[b]					Smyth et al. (2005)
100	0.56	43.73[b]					Smyth et al. (2005)
100	0.45	43.72[b]					Smyth et al. (2005)
100	0.44	43.69[b]					Smyth et al. (2005)
100	0.34	43.69[b]					Smyth et al. (2005)
100	0.1	43.68[b]					Smyth et al. (2005)
100	0	43.68[b]					Smyth et al. (2005)
97	0.89		124.4(4)[a]	75.3(3)			Jacobsen et al. (2008)

a - values are for Ks

b - values measured at high temperature

Table 3: **Wadsleyite**

Mg/(Mg+Fe)	$wt\%$ **water**	V_0	K_{T0}	G_0	dK/dP	dG/dP	**reference**
100	2.5(3)	40.59	155(2)		4.3[b]		Yusa and Inoue (1997)
100	2.4(2)						Inoue et al. (2004)
100	1		152(6)		6.5(20)		Holl et al. (2008)
100	0.005	40.52	173(5)		4.1(15)		Holl et al. (2008)
100	0.005	40.51	174(1)		4[b]		Holl et al. (2008)
100	0.38	40.59	161(4)		4.9(11)		Holl et al. (2008)
100	0.38	40.58	164.7(12)		4[b]		Holl et al. (2008)
100	1.18	40.63	158(4)		4.2(9)		Holl et al. (2008)
100	1.18	40.63	159.2(8)		4[b]		Holl et al. (2008)
100	1.66	40.69	154(4)		5.4(11)		Holl et al. (2008)
100	1.66	40.68	160.3(12)		4[b]		Holl et al. (2008)
100	0.37	40.55	165.4(9)[a]	108.6(6)			Mao et al. (2008a)
100	0.84	40.58	160.3(7)[a]	105.3(6)			Mao et al. (2008a)
100	1.66	40.66	149.2(6)[a]	98.6(4)			Mao et al. (2008a)
100	0.84				4.1(1)[a]	1.4(1)	Mao et al. (2008b)
100	2.8	40.85	137(5)		4.5(3)		Ye et al. (2010)
100	2.8	40.77	147(2)		4[b]		Ye et al. (2010)
100	1						Smyth and Jacobsen (2006)
89	1.93		156.2(5)[a]	98.0(3)	4.8(1)	1.9(1)	Mao et al. (2011)

a - values are for Ks
b - fixed values

Table 4: **Ringwoodite**

Mg/(Mg+Fe)	$wt\%$ **water**	V_0	K_{T0}	G_0	dK/dP	dG/dP	**reference**
100	0.74	39.54					Smyth et al. (2003)
100	0.74	39.54					Smyth et al. (2003)
100	2.00(19)	39.62					Kudoh et al. (2000)
100	2.2(2)	39.69	155(4)	107(3)			Inoue et al. (1998)
100	2.33(11)	39.9	166.2(5)[a]	107.6(3)	4.4(1)	1.7(1)	Wang et al. (2006)
100	2.34	39.9	165.8(5)[a]	107.4(3)			Wang et al. (2003)
100	2.4						Ye et al. (2009)
100	2.5(3)	39.86	159(7)		6.7(7)		Ye et al. (2012)
100	2.5(3)	39.75	161(4)		5.4(6)		Ye et al. (2012)
100	2.5(3)		160(2)		6.2(3)		Ye et al. (2012)
100	2.8(2)	39.83	148(1)		5[b]		Yusa et al. (2000)
91	1	39.96	176(7)[a]	103(5)			Jacobsen et al. (2004)
90	0.79	39.93	174.6(27)		6.2(6)		Manghnani et al. (2005)
90	0.93	39.94	169.0(34)		7.9(9)		Smyth et al. (2003)
90	1		177(4)[a]	103.1(9)	5.3(4)	2.0(2)	Jacobsen and Smyth (2006)
89.7	0.86	39.86					Smyth et al. (2003)
89.2	0.79	39.86					Smyth et al. (2003)
88.5	0.92	39.92					Smyth et al. (2003)
87.1	1.07	40.08					Smyth et al. (2003)
86	1.1		175(1)[a]	106(1)	4.0(1)	1.6(1)	Mao et al. (2012)
49	0.7	40.9	186.5(9)		4[b]		Ganskow et al. (2010)
61	0.37	40.58	184.1(7)		4[b]		Ganskow et al. (2010)

a - values are for Ks
b - fixed values

B Debye temperature and Helmholtz free energy

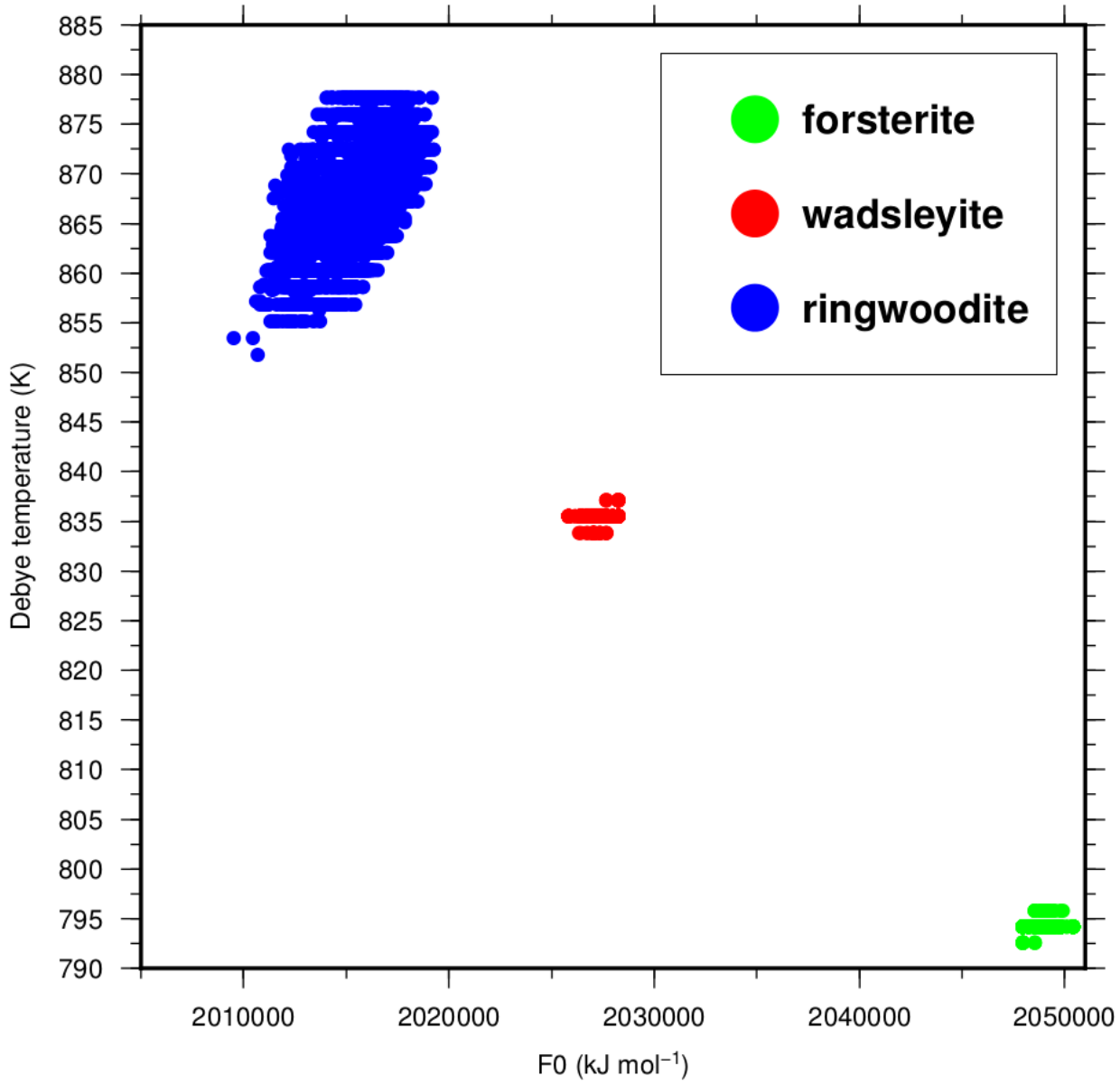

Debye temperatures and F0 values for forsterite, wadsleyite and ringwoodite from our hydrous models.